

# Local imperfect feedback control in non-equilibrium biophysical systems enabled by thermodynamic constraints

Carlos Floyd,<sup>\*</sup> Aaron R. Dinner, and Suriyanarayanan Vaikuntanathan<sup>†</sup>

*The Chicago Center for Theoretical Chemistry, The University of Chicago, Chicago, Illinois 60637, USA*

*Department of Chemistry, The University of Chicago, Chicago, Illinois 60637, USA and*

*The James Franck Institute, The University of Chicago, Chicago, Illinois 60637, USA*

(Dated: July 11, 2025)

Understanding how biological systems achieve robust control despite relying on imperfect local information remains a challenging problem. Here, we consider non-equilibrium models which are generically used to describe natural and synthetic biological processes, such as gene regulation and protein conformational dynamics, and investigate their capacity for effective control using imperfect local feedback mechanisms. We derive a thermodynamic constraint on the response of non-equilibrium steady-state properties to changes in the driving forces. We show that this constraint enables linear, local, and easily implementable feedback rules to achieve environmental tracking and adaptation without consideration of network topology. In particular, we demonstrate that local stability of these feedback dynamics implies global stability for systems with one or two chemical regulators, regardless of the network topology. For higher-dimensional systems, global stability is not guaranteed. However, in part due to simplifications in attractor landscapes implied by our thermodynamic constraint, we find the basin of attraction remains significantly larger than would be expected from linear approximation alone. Our findings provide insight into how biological and synthetically engineered systems can respond effectively to environmental changes given only minimal feedback, without highly engineered interactions or precise parameter tuning.

## I. INTRODUCTION

A common challenge in learning, training, or adaptation tasks is reliance on imperfect or incomplete information about the system. Despite this difficulty, there are several notable examples where such information is used successfully. For instance, the adaptive immune system must rely on imperfect spatiotemporally local information, such as estimates of binding affinities between antigens and receptors on cells [1]. Despite such limitations, these and other biological responses appear to make near-optimal use of available information, even in time-varying environments [1–5]. How imperfect local information can guide control in complex environments remains an important and open question.

A key difficulty in answering this question is that many biological control and adaptation tasks occur in non-equilibrium settings, where there are fewer thermodynamic guarantees on stability compared to equilibrium settings [1, 6–8]. Furthermore, given the high dimensionality and complexity of biological systems, one might expect that different initial conditions would lead to different (meta)stable states, i.e., local attractors, making optimization sensitive to the precise mechanism of feedback control. Here, we prove a general thermodynamic constraint on the response of steady states to changes in driving forces for a broad class of non-equilibrium processes. Specifically, we show that a steady state’s partial derivative with respect to the driving force maintains a fixed sign for all values of the force, which we refer to

a monotonicity property. This is akin to the fixed-sign properties of partial derivatives of free energy that provide thermodynamic stability in equilibrium settings [9]. As a consequence of this constraint, the solution space for complex control problems can be surprisingly simple, often featuring a global attractor.

We establish this constraint using a graph-theoretic proof within the context of Markov jump processes, a ubiquitous modeling framework encompassing many biophysical processes (Figures 1 and 2). We then leverage this monotonicity property to show how non-equilibrium systems can effectively mount dynamical responses to time-dependent environmental changes using minimal, linear feedback connections between observables defined on node probabilities and non-equilibrium driving forces. We discuss how such linear feedback rules can occur and be useful in biological contexts (Figure 3) [10, 11]. Indeed, they can be viewed as integral feedback control rules which, due to our thermodynamic constraints, are effective for a wide range of topologies and interactions without the need for any fine tuning or engineering [12]. In line with the concept of imperfect gradients used in machine learning [13–15], these linear feedback connections serve as local and fixed approximations to globally stable feedback mechanisms which would require complete (non-local) and instantaneous information about the network state.

We demonstrate the utility of these simple feedback connections in two tasks: one where the system updates an internal model of the environmental state and another where it adapts to an environmental perturbation by returning to a set point. Importantly, for systems with one or two chemical regulators, our monotonicity constraint implies the global stability of these minimal feedback con-

<sup>\*</sup> csfloyd@uchicago.edu

<sup>†</sup> svaikunt@uchicago.edu

nections for any arbitrary network topology; no specific motifs or modular designs are necessary [16]. Our results, which are enabled by the thermodynamic constraints we derive, can be viewed as simple, easily implementable, and local learning rules that can be used to track changing environmental conditions. Finally, we explore how guarantees on stability change as the number of chemical regulators in the system increases. Such guarantees could facilitate the design of next-generation synthetic biochemical feedback systems [11, 12, 17–23].

## II. A NEW THERMODYNAMIC CONSTRAINT ON THE RESPONSE OF FAR-FROM-EQUILIBRIUM PROCESSES

In many biological and physical systems, sustained external forcing keeps the system away from equilibrium. A central question is how the steady-state probabilities change as a function of an applied driving force [24–26]. Here we model systems as Markov jump processes over discrete sets of  $N_n$  states. Transitions between states are Poisson processes, with the rate from state  $j$  to state  $i$  given by

$$W_{ij} = e^{E_j - B_{ij} + F_{ij}(\alpha_a)/2}, \quad (1)$$

where  $E_j$  represents an energy level associated with state  $j$ ,  $B_{ij} = B_{ji}$  represents an equilibrium barrier height and  $F_{ij} = -F_{ji}$  represents non-conservative driving forces such as unbalanced chemical potentials or enzymatic catalysis [24]. These  $F_{ij}$  affinity-like terms break detailed balance and can drive the system far from equilibrium. Although  $F_{ij}$  could depend in various ways on the  $a^{\text{th}}$  input variable  $\alpha_a$ , for simplicity we set  $F_{ij}(\alpha_a) = F_{ij}^0 + \alpha_a$  and represent by  $\alpha_a$  additive contributions to the non-equilibrium driving forces along some of the  $N_e$  edges. The state of the system is described by the probability vector  $\mathbf{p}(t) \in \mathbb{R}^{N_n}$  which evolves according to the master equation  $\dot{\mathbf{p}} = \mathbf{W}(\boldsymbol{\alpha}; \boldsymbol{\theta})\mathbf{p}$ , where  $\boldsymbol{\alpha} \in \mathbb{R}^{N_a}$  represents the additive contributions to the driving forces and  $\boldsymbol{\theta} \in \mathbb{R}^{N_n + 2N_e}$  represents the rate parameters  $E_j$ ,  $B_{ij}$ , and  $F_{ij}^0$ . Under the assumption of ergodicity, the system relaxes to a unique steady state  $\boldsymbol{\pi}(\boldsymbol{\alpha}; \boldsymbol{\theta}) = \lim_{t \rightarrow \infty} \mathbf{p}(t)$ . Observables  $C$  that are functions of the state, such as the weighted average occupancy of a set of nodes, can be computed as  $C(\mathbf{p}) = \sum_m w_m p_m$ , with  $w_m$  denoting the weight of node  $m$ .

Our central result is the derivation of a thermodynamic constraint on the non-equilibrium response, i.e., the derivative  $\partial C / \partial \alpha_a$  which quantifies how  $C$  changes as a function of the driving force  $\alpha_a$ . We demonstrate for a broad class of observables (including weighted averages) that when all other parameters in the network are held fixed, this derivative maintains a fixed sign across the range of  $\alpha_a$ . In other words, the observable  $C$  responds strictly monotonically to changes in  $\alpha_a$ . This fixed sign property of a non-equilibrium response is analogous to

the conditions imposed by the convexity of free-energy derivatives in equilibrium thermodynamics [9].

As described in Methods, the derivation of this monotonicity constraint relies on a graph-theoretic analysis using the matrix-tree theorem [27]. In this approach, the steady-state probability  $\pi_m$  at an arbitrary node  $m$  is expressed as a sum over directed spanning trees of the network with each tree weighted by the product of the transition rates along its edges. Using a theoretical technique called “tree surgery” [24] (see SI Figure 7) we establish an equality, illustrated in Figure 2, among the weights of directed spanning trees rooted at node  $m$  and those rooted at the nodes  $i$  and  $j$  adjacent to the driven edge regulated by  $\alpha_a$ . By differentiating the expression for  $\pi_m$  with respect to the driving force  $\alpha_a$  and applying the equality that we derived, we obtain an expression of the form (cf. Equation 29)

$$\frac{\partial \pi_m}{\partial \alpha_a} = x_m G(\alpha_a), \quad (2)$$

where  $G(\alpha_a)$  is a node-independent and strictly positive function of  $\alpha_a$ . Consequently, the sign of  $\partial \pi_m / \partial \alpha_a$  is determined solely by the prefactor  $x_m$ , which depends on the network structure and is independent of  $\alpha_a$  (see Figure 2B). This sign constraint further implies that the derivative of any linear observable  $C(\boldsymbol{\pi}) \equiv \sum_m w_m \pi_m$ , given by

$$\frac{\partial C(\boldsymbol{\pi})}{\partial \alpha_a} = \sum_m w_m \frac{\partial \pi_m}{\partial \alpha_a} = G(\alpha_a) \sum_m w_m x_m, \quad (3)$$

also retains a fixed sign as  $\alpha_a$  is varied. We note that more general observables, such as non-linear functions of  $\boldsymbol{\pi}$ , can be defined which also have the fixed-sign property (replacing  $w_m$  by the more general  $\partial C / \partial \pi_m$ ), but for simplicity we focus here on linear observables such as weighted averages. In Methods we show that monotonicity can also be established for the response of steady-state probabilities to changes in  $E_i$ ,  $B_{ij}$ , and  $W_{ij}$ . The results established below for feasibility of control using  $F_{ij}$  parameters as regulated variables thus also apply to control based on these other parameters.

In the next section, we utilize this monotonicity property to design and analyze control strategies for non-equilibrium systems. We argue how this fixed-sign property could have implications for the ability of non-equilibrium systems to track and adapt to environmental changes using simple local rules.

## III. THERMODYNAMIC CONSTRAINTS ENABLE SIMPLE RULES FOR TRACKING AND ADAPTATION

Having established a thermodynamic constraint on the monotonicity of the non-equilibrium response  $C(\alpha_a)$ , we now illustrate how this property enables Markov jump

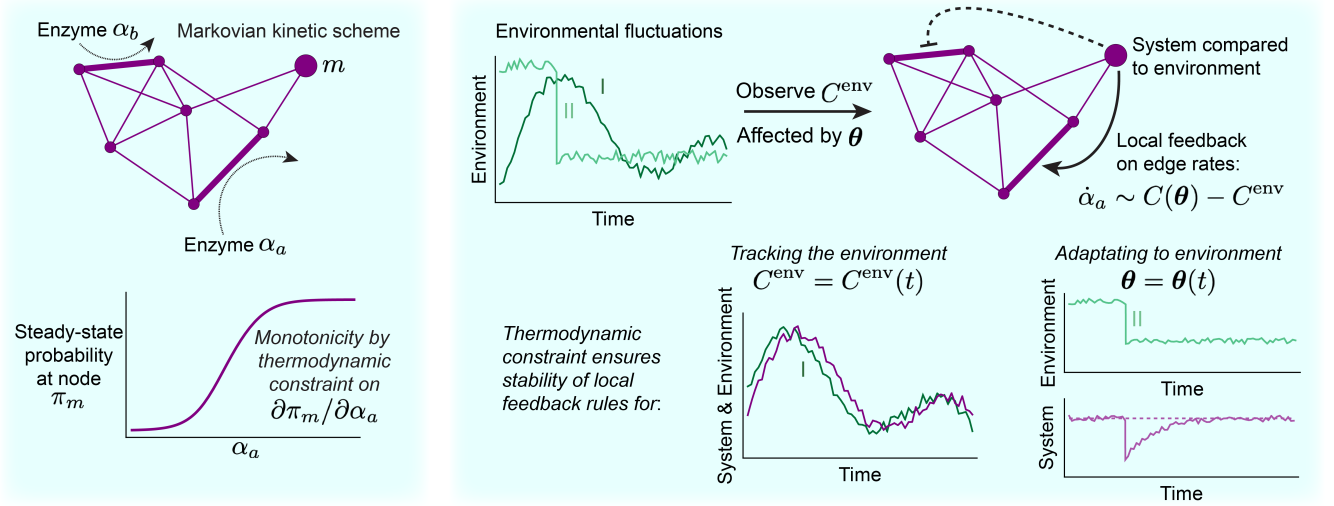


FIG. 1. **A thermodynamic constraint on non-equilibrium response enables control of Markov jump processes by local feedback connections.** *Left:* The response of the non-equilibrium steady-state probability  $\pi_m$  at node  $m$  to a change in a driving force  $\alpha_a$  is strictly monotonic. This manifests as a partial derivative  $\partial\pi_m/\partial\alpha_a$  having a fixed sign across the range of  $\alpha_a$ . *Right:* This monotonicity property enables dynamical control using simple local linear feedback loops even from initial conditions far away from the desired fixed points. We consider a system-environment decomposition in which fluctuating environmental variables enter as external functions in the feedback for driving forces or in the network parameters. Depending on the nature of the feedback, the system can track the environmental variables or adapt to perturbations by returning to a set point.

processes to exhibit robust tracking and adaptation behaviors via local imperfect feedback loops. We consider two generic scenarios (see Figure 1): one in which a network observable tracks a time-dependent environmental signal, and another in which environmental perturbations alter the network rates, necessitating homeostatic maintenance of a network observable at a set point.

While devising general control strategies for non-equilibrium chemical dynamics is inherently challenging [11, 12, 19–23, 28], we show that a simple local rule can suffice for effective control in a wide range of settings. In this rule we update the affinity  $\alpha_a$ , which enters additively to  $F_{ij}$  along a particular regulated edge, according to

$$\dot{\alpha}_a = S_{a1} (C_1(\mathbf{p}) - C_1^{\text{env}}), \quad (4)$$

where  $S_{a1}$  is a fixed scalar constant,  $C_1$  denotes the current value of a network observable, and  $C_1^{\text{env}}$  is its environmentally determined target value. We refer to Equation 4 as local because only one network observable, rather than the whole network state, is used to provide feedback to  $\alpha_a$ . Depending on the sign of  $S_{a1}$ , the term proportional to  $C_1^{\text{env}}$  represents either a degradation or production term for the affinity  $\alpha_a$ , while the term proportional to  $C_1(\mathbf{p})$  represents a process with the opposite effect. We emphasize that Equation 4 is linear in a single observable  $C_1(\mathbf{p})$ . While this simple linear form might be expected to achieve control close to a fixed point, we show in the subsequent sections that the thermodynamic con-

straint derived above enables this linear form to achieve control and adaptation globally.

Updates of the form implied by Equation 4 may naturally arise in various biological contexts. For instance, in transcriptional circuits, gene products can interfere with the transcription factors (TFs) that bind to promoter regions [29]. In the schematic four-state model shown in Figure 3, the concentration of a gene product (GP) is, in the quasi-steady-state limit, proportional to the occupancy of both states bound to RNA polymerase (RNAP). The GP then degrades the TF according to

$$\frac{\partial[\text{TF}]}{\partial t} = -D[\text{GP}] + k^{\text{env}}, \quad (5)$$

where  $D$  is a first-order degradation rate. We assume a saturating kinetic effect of degradation giving it a first order dependence on the concentration  $[\text{GP}]$ , and  $k^{\text{env}}$  represents an environmentally determined production rate which may include contributions from nuclear transport and transcription. By interpreting  $\alpha_a$  as being modulated by  $[\text{TF}]$  which scales the pseudo-first-order transitions from the states on the left to those on the right in Figure 3, and  $[\text{GP}]$  as  $C_1$ , one can see that this model is physically equivalent to Equation 4. This phenomenology incorporates feedback from a network observable (the weighted occupancy of RNAP-bound DNA) into the rate of a Markov process [10, 11, 16]. Although our update rules resemble widely used integral feedback mechanisms, they differ in a key aspect: rather than relying on spe-

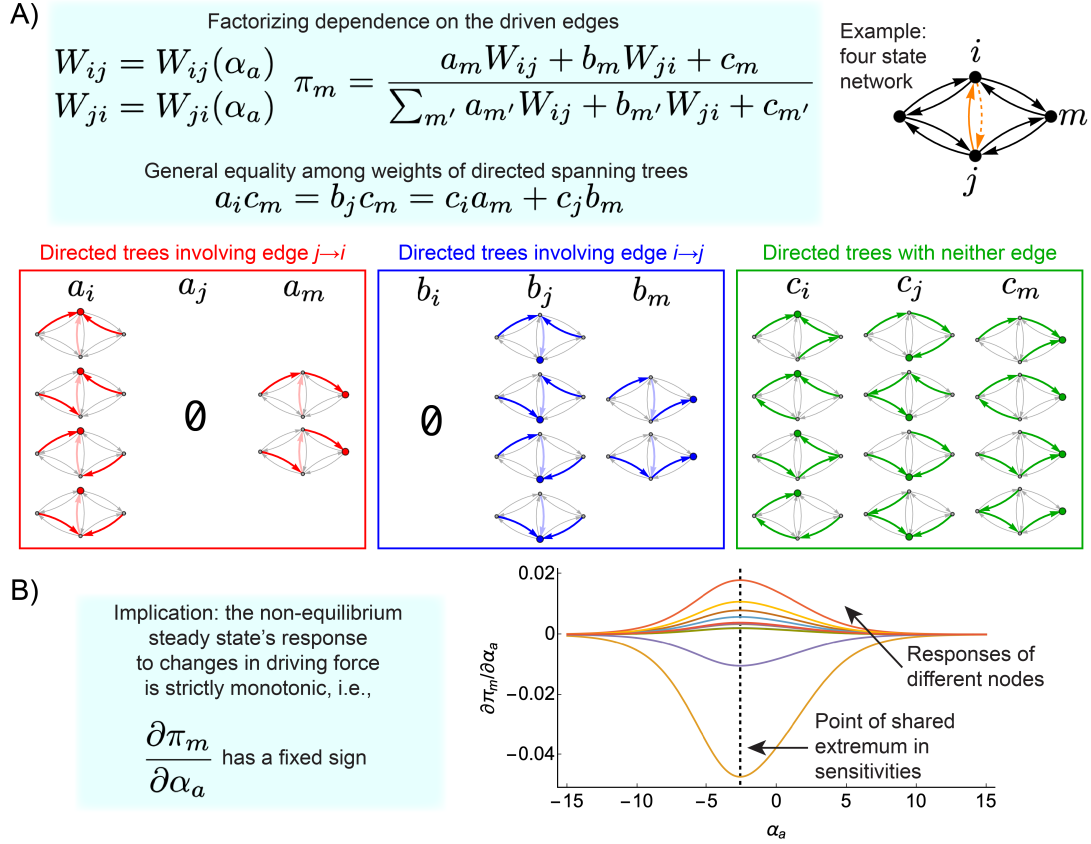


FIG. 2. **The non-equilibrium response to change in driving force is strictly monotonic.** A) Illustration of the factorization of the matrix-tree expression for  $\pi_m$  into terms that include  $W_{ij}$ ,  $W_{ji}$ , or neither of these. B) For the graph depicted in Figure 4A, the steady-state probabilities of all nodes  $m$  as  $\alpha_a$  is varied. Partial derivatives  $\partial \pi_m / \partial \alpha_a$  are shown, colored according to the color of each node  $k$  in the graph. The dashed vertical line indicates the shared value of  $\alpha_a$  for each node where the partial derivative is extremized. See the Methods for definitions and elaborations of these results.

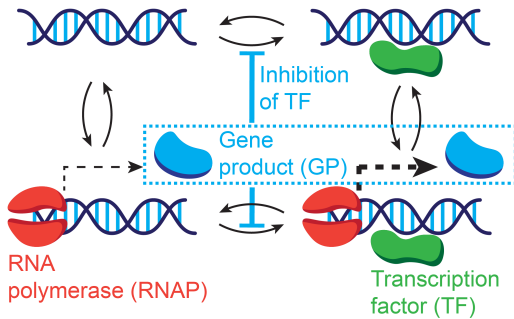


FIG. 3. **Example of local biomolecular feedback control.** Schematic illustration of local feedback regulation of a DNA transcription site by the gene product of transcription.

cific assumptions about network topology or interaction details to ensure stability, our formulation is grounded in thermodynamic constraints. These constraints provide general guarantees of stability that hold regardless of the

particular structure or complexity of the underlying network [12, 21].

While our current framework is most directly applicable to a system of non-equilibrium unimolecular (i.e., first-order or pseudo-first-order) reactions, we anticipate that it can be extended to certain classes of bimolecular reactions as well. In Refs. 30–32, for example, it is described how under approximations like timescale separation, bimolecular reaction networks or enzyme catalyzed reactions describing the dynamics of chemical concentrations can be cast into effective linear forms for which the matrix-tree theorem applies and our thermodynamic constraint holds. These works also account for processes like degradation and synthesis within the reaction network (not just through the feedback rules), broadening the set of biological scenarios to which our results apply.

We next proceed to show how systems with the local feedback rule in Equation 4 achieve control in a range of settings. We analytically and numerically establish that local stability of the dynamics in Equation 4 implies global stability when only one or two driving forces are regulated, regardless of the complexity of the over-



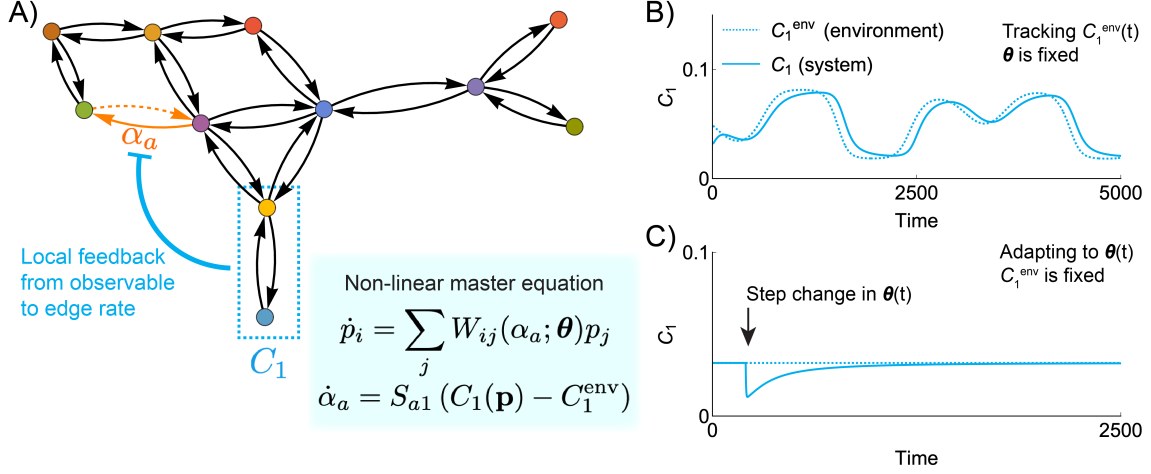


FIG. 4. **Tracking environmental variables in one dimension using imperfect local feedback connections.** A) Markov network labeled with the regulated driving force  $\alpha_a$  and the environmentally tracked observable  $C_1$ , defined as an average of the instantaneous probabilities for the nodes in the dashed box. The constant  $S_{a1} = -1$  is negative (inhibitory) for this connection. B) Plot of the environmental trajectory of  $C_1^{\text{env}}(t)$  which is tracked by the system observable  $C_1(t)$  using the local imperfect feedback connection. C) Same as panel B, but for the case when  $C_1^{\text{env}}$  is fixed in time while the system's rate parameters  $\theta(t)$  undergo a step change. The change in  $\theta$  here is obtained by decrementing the value of  $F_{ij}$  on the edge between the blue and yellow nodes.

all network. Despite the thermodynamic constraint on monotonicity failing as multiple edges are tuned simultaneously in systems with high-dimensional feedback, we give numerical results and heuristic arguments which show that similar robust behavior persists. The thermodynamic constraint on response provides far greater stability to the system than would be expected naively given the simple linear form of Equation 4.

#### A. Tracking and adaptation with one feedback loop: global stability of linear feedback rule due to constraints on non-equilibrium response

We first consider a control problem with one regulated driven edge, i.e.,  $N_\alpha = 1$ . As mentioned previously, such feedback regulation can be expected to occur routinely in biological systems. Figure 4A illustrates the random graph used in this section, with the regulated edge and feedback observable  $C_1$  labeled. The local stability of the nonlinear Markov dynamics,  $\dot{\mathbf{p}} = \mathbf{W}(\alpha_a)\mathbf{p}$  combined with Equation 4, depends on the value of  $S_{a1}$ . We first consider an adiabatic limit in which the network is always at steady state for the current value of  $\alpha_a(t)$ , i.e.,  $\mathbf{p}(t) = \pi(\alpha_a(t))$ . In this limit Equation 4 reads

$$\dot{\alpha}_a(t) = S_{a1}(C_1(\pi(\alpha_a(t))) - C_1^{\text{env}}). \quad (6)$$

Local stability of these dynamics is ensured if  $S_{a1}$  is chosen to have the opposite sign of  $\partial C_1 / \partial \alpha_a$  evaluated at the fixed point  $C_1(\pi(\alpha_a^{\text{env}})) = C_1^{\text{env}}$ . Considering the region of validity of a Taylor expansion to first order, the size of the basin of attraction is expected to be roughly pro-

portional to this gradient. However, the non-equilibrium constraint on the fixed sign of  $\partial C_1 / \partial \alpha_a$  ensures that  $S_{a1}$  and  $-\partial C_1 / \partial \alpha_a$  share the same sign for any value of  $\alpha_a$ . Consequently, the dynamics are also globally stable (see SI Figure 9) due to our thermodynamic constraint, with an infinitely-sized basin of attraction.

In an intermediate regime outside the adiabatic limit the dynamics are also stable provided the feedback timescale, determined by the magnitude of  $S_{a1}$ , is not significantly faster than the relaxation time of the Markov process  $\mathbf{W}(\alpha_a)$ . We illustrate this in Figure 4C, in which  $C_1(\mathbf{p}(t))$  tracks a time-dependent environmental signal  $C_1^{\text{env}}(t)$  outside of the adiabatic limit. These results show that linear feedback based on local information enables biochemical networks with arbitrary topologies to maintain an internal representation which non-adiabatically tracks a time-dependent environmental variable.

We next consider the ability of the network to adapt to environmental perturbations outside the adiabatic limit using the local imperfect feedback connection in Equation 4. We fix the environmental feedback variable  $C_1^{\text{env}}$  as a desired set point of the internal variable  $C_1(\mathbf{p}(t))$  and subject the network to a step change in the parameters  $\theta(t)$  of its rate matrix  $\mathbf{W}(\alpha_a, \theta)$ . For concreteness we illustrate this by changing the value of  $F_{ij}$  along a different (non-regulated) edge in the network, but other perturbations are possible. Under the new parameters  $\theta$  the network will have a quantitatively different non-equilibrium steady-state response function  $C_1(\pi(\alpha_a; \theta))$ , but provided that this new response still intersects  $C_1^{\text{env}}$  for some value of  $\alpha_a$  and its derivative  $\partial C_1 / \partial \alpha_a$  does not change sign, the dynamics in Equation 4 will recover the

fixed point  $C_1(\alpha_a; \theta) = C_1^{\text{env}}$ . This is illustrated in Figure 4C, suggesting that the thermodynamic constraint enables imperfect local rules to perform adaptation tasks in arbitrary biochemical networks. The network structure can affect the allowed range of the adaptive response, however. In SI Figure 10 we show an example of a network which perfectly adapts only for a certain range of perturbation sizes, and in SI Figure 11 we show an example of a network which perfectly adapts for any perturbation size. This ability of steady states to adapt with arbitrary network topologies using simple linear feedback rules on any regulated edges can be contrasted with previous works which consider specially designed motifs or network substructures, or require various assumptions about the system's response [6, 7, 12, 16, 19–23, 33].

Far outside the adiabatic limit, when the feedback  $S_{a1}$  is very large in magnitude, oscillatory steady states may arise instead of fixed points (see SI Figure 12). This phenomenon is analogous to oscillatory instabilities observed in other control systems with excessive feedback gain [11, 34], and it can be understood by analyzing the eigenvalues of the coupled dynamics. For simplicity, in the remainder of this paper we focus on the adiabatic limit. In SI Figure 9 we also compare the dynamics under the local imperfect feedback to those under non-local feedback dynamics, where a Jacobian element is used in place of  $S_{a1}$  in Equation 4. This feedback is non-local because evaluating the Jacobian element requires instantaneous information from the whole network. As explained in the Methods, these non-local dynamics are guaranteed to be globally stable because they minimize a Lyapunov function. Although both the local and non-local dynamics are globally stable for  $N_\alpha = 1$ , they have different trajectories toward the fixed point.

### B. Tracking with two feedback loops: global stability of linear feedback rule due to constraints on non-equilibrium response

We now consider the feasibility of control using local imperfect feedback on two regulated edge rates,  $\alpha_a$  and  $\alpha_b$ , i.e., when  $N_\alpha = 2$ . Introducing control over an additional driving force presents a challenge: for the non-equilibrium thermodynamic constraint on the sign of  $\partial C / \partial \alpha_a$  to hold, all other network parameters must remain fixed. If they vary, the quantities in Equations 17–19 may change sign, causing the derivative to do so as well. Despite this, we provide numerical evidence and analytical arguments demonstrating that local stability also implies global stability for the local imperfect feedback dynamics in two dimensions.

Figure 5A shows the Markov network from Figure 4A, now with an additional regulated driving force  $\alpha_b$ . Feedback to these two affinities can be implemented in two general ways: (a) using two unique observables,  $C_1$  and

$C_2$ , i.e.,

$$\dot{\alpha}_a = S_{a1} (C_1 - C_1^{\text{env}}) \quad (7)$$

$$\dot{\alpha}_b = S_{b2} (C_2 - C_2^{\text{env}}), \quad (8)$$

or (b) redundantly using the same observable, i.e.,

$$\dot{\alpha}_a = S_{a1} (C_1 - C_1^{\text{env}}) \quad (9)$$

$$\dot{\alpha}_b = S_{b1} (C_1 - C_1^{\text{env}}). \quad (10)$$

These two approaches give rise to qualitatively different feedback dynamics. When two distinct observables are used, the system typically possesses a unique fixed point, located at the intersection of the contours  $C_1(\alpha_a, \alpha_b) = C_1^{\text{env}}$  and  $C_2(\alpha_a, \alpha_b) = C_2^{\text{env}}$ , which coincide with the nullclines  $\dot{\alpha}_a = 0$  and  $\dot{\alpha}_b = 0$ . In the SI we demonstrate that this fixed point is indeed unique, meaning there are no other isolated roots of the equations  $\dot{\alpha}_a = 0$  and  $\dot{\alpha}_b = 0$ . By appropriately selecting the values of  $S_{a1}$  and  $S_{b2}$ , the fixed point can be rendered locally stable. Figure 5B illustrates this local stability through several convergent trajectories and a vector field indicating the direction of local flow.

If, instead, the same observable  $C_1$  is redundantly used as feedback for both  $\alpha_a$  and  $\alpha_b$ , the system possesses a one-dimensional manifold of fixed points defined by the solution space of  $C_1(\alpha_a, \alpha_b) = C_1^{\text{env}}$ . Biologically, this redundant feedback could correspond to a single DNA transcription region encoding two gene products which modulate two transcription factor activities  $\alpha_a$  and  $\alpha_b$  in a shared regulatory network (cf. Figure 3). With appropriately chosen  $S_{a1}$  and  $S_{b1}$  the trajectories converge stably toward the one-dimensional manifold of fixed points (Figure 5C). This redundancy can be biologically advantageous by simplifying the flow fields and enabling more direct convergence to  $C_1 = C_1^{\text{env}}$ , minimizing large excursions in  $\alpha$  space. Although one-dimensional solution manifolds are always a feature of redundant feedback connections, we show in the Methods that they can also emerge for certain “low-rank” choices of two distinct observables,  $C_1$  and  $C_2$ . Additionally, we note that adaptation remains possible in the case of two-dimensional control. For brevity we do not show this here, but we illustrate this in the more general high-dimensional setting in the next section.

Figure 5D illustrates a numerical search over random graphs and random initial conditions around a locally stable fixed point. In every case, the initial conditions converge to the fixed point, suggesting that the basins of attraction for these fixed points extend throughout the entire domain sampled, implying that the fixed points are globally stable (see SI Figure 8 for larger sampling regions). Although rigorously proving global stability is challenging, it is plausible due to the fact that the nullclines are significantly limited by the non-equilibrium thermodynamic constraint. Specifically, the uniqueness of the isolated fixed points ensures that no two nullclines can intersect more than once (see SI Methods for a proof

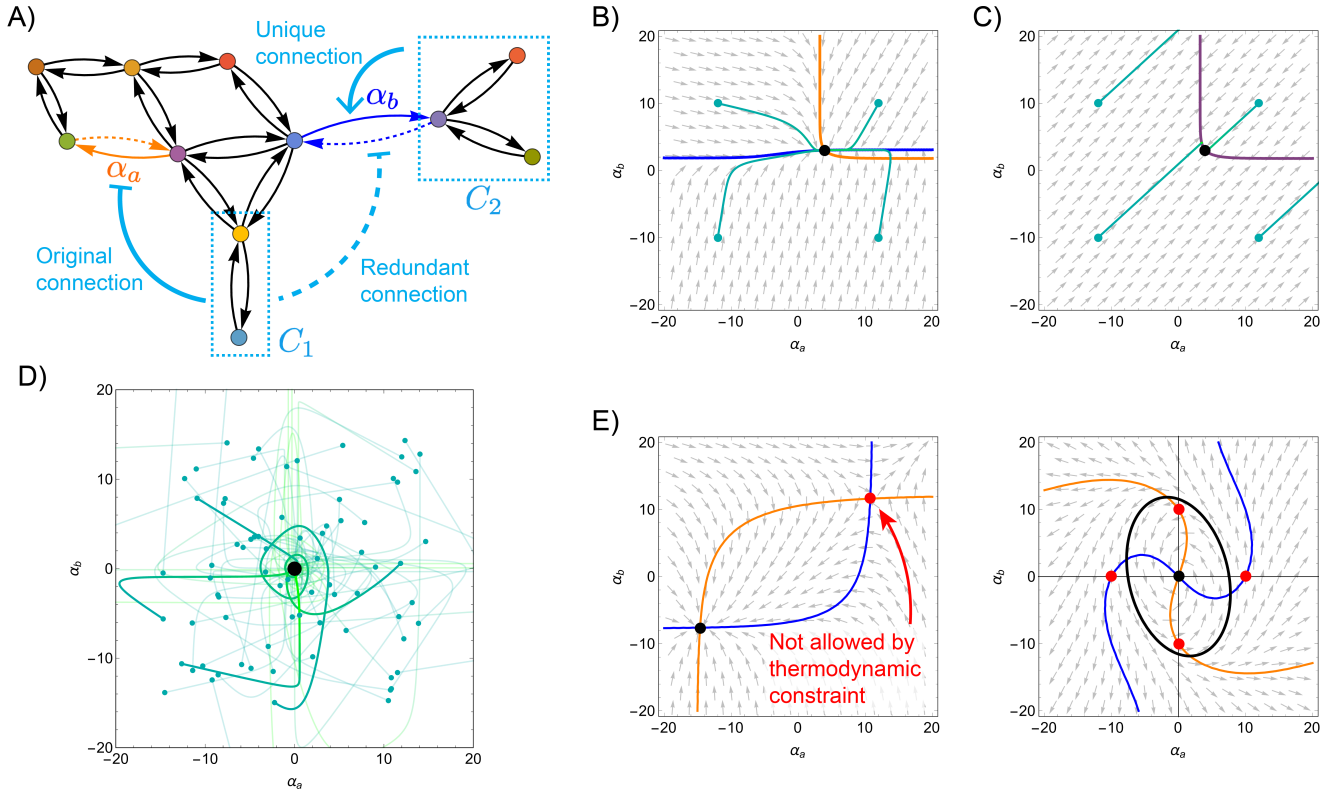


FIG. 5. **Stability of imperfect local feedback connections in two dimensions.** A) The same Markov network as in Figure 4A, redrawn to indicate two new feedback connections. The first, drawn as a solid line, connects the driving force  $\alpha_b$  to a new observable,  $C_2$ , which is the average of the steady-state probabilities of the nodes in the dashed box. The second, drawn as a dashed line, connects  $\alpha_b$  to the same observable  $C_1$  that is connected to  $\alpha_a$ . B) Phase plane for unique connections under the adiabatic dynamics. The nullclines for  $\dot{\alpha}_a$  and  $\dot{\alpha}_b$  are drawn in orange and blue, respectively, and arrows are drawn indicating the direction (but not magnitude) of flow field. Four trajectories, colored from dark to light green in time and with initial values as points, are also plotted. The black point is the stable fixed point. C) Same as panel B, but for the redundant set of connections. The nullclines for  $\alpha_a$  and  $\alpha_b$  overlap in this case. D) For randomly sampled graphs with  $N_n = 11$  and  $N_e = 13$ , plots of trajectories from randomly sampled initial conditions. All sampled trajectories converge to the locally stable fixed point at  $\alpha^{\text{env}} = \mathbf{0}$  (which we set the same for all graphs). E) Schematic illustration of how the thermodynamic constraints on monotonicity of the observables along axes of  $\alpha_a$  and  $\alpha_b$  and their unique intersections prevents the formation of certain unstable structures such as limit cycles and saddle points. In the phase portraits of these toy dynamical systems, red points illustrate nullcline features would be prevented by the thermodynamic constraint in our Markov network feedback control.

of unique intersections), preventing the formation of saddle points with unstable manifolds (Figure 5E) [35, 36]. Furthermore, the constraint on the monotonicity of the observables ensures that the nullclines intersect any vertical or horizontal line in  $\alpha$  space at most once. This precludes the formation of unstable limit cycles around the stable fixed point. These restrictions on the formation of unstable structures suggest that the two-dimensional dynamics, which in general are significantly more constrained than three-dimensional systems [37], are globally stable as observed numerically. Thus, although simultaneously modifying two driving forces can result in incorrect sign estimates  $S_{a1}$  and  $S_{b1}$  in certain regions of  $\alpha$  space, the topologically simple structure of the nullclines, enforced by the non-equilibrium thermodynamic constraint, ultimately guarantees the global stability of

the local feedback dynamics.

### C. Simple rules for tracking and adapting to high dimensional signals

Lastly, we consider the feasibility of control in scenarios where multiple signals ( $N_\alpha > 2$ ) must be tracked, necessitating a correspondingly large number of feedback loops. We formally define the feedback dynamics for this general case in the Methods section. An example graph with  $N_\alpha = 3$  is depicted in Figure 6A [10, 38], in which we introduce a third driving affinity,  $\alpha_c$ , along with feedback from three distinct network observables. To illustrate the range of dynamical behaviors in this higher-dimensional system, we consider two different placements of the first

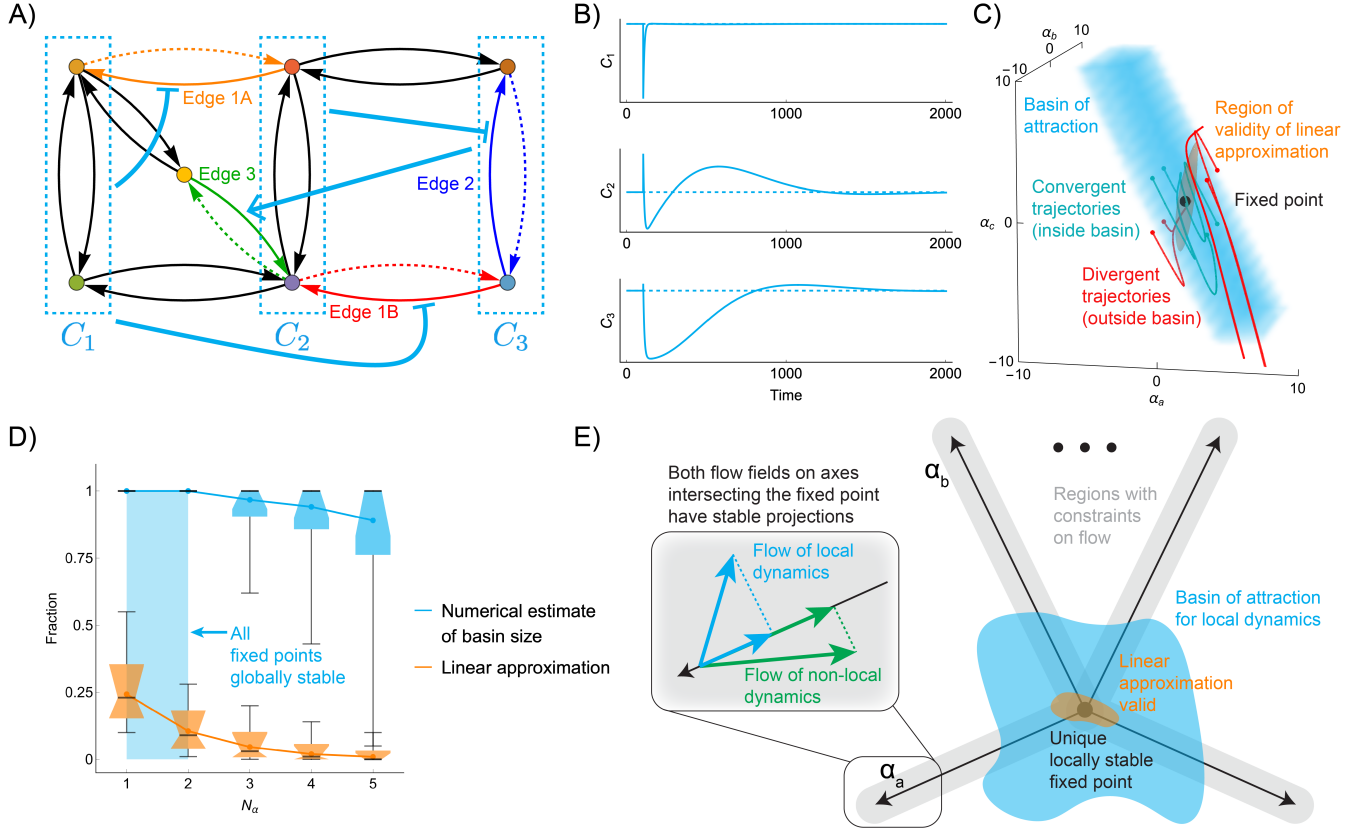


FIG. 6. **Control in higher dimensions.** A) A Markov network loosely based on a biologically relevant transcriptional motif [10, 38]. Three network observables  $C_1$ ,  $C_2$ , and  $C_3$  defined as weighted averages of the enclosed nodes are shown. These feed back to three regulated edge rates. In panel B edge 1A is regulated through feedback, and in panel C edge 1B is regulated. B) Adaptation of the three observables to a step change in the network parameters  $\theta$ , which we take here to be a random perturbation to all of the nodes' energy levels  $E_i$ . C) Depiction of a locally stable fixed point which is not globally stable. The basin of attraction, comprising all initial conditions which converge asymptotically to the fixed point, is drawn as a cyan cloud. Representative trajectories from inside and outside this basin are drawn. For comparison, we draw the contour  $\|\mathbf{J}(\alpha) - \mathbf{J}(\alpha^{\text{env}})\|_F = 0.025$  of the Frobenius norm of the deviation of the Jacobian matrix from its value at the fixed point, which serves as a measure of the validity of the linear approximation to the Jacobian. D) Results of numerically sampling random graphs with  $N_n = 11$  and  $N_e = 13$  and determining the fraction of trajectories in a hypercube of edge length  $\Delta\alpha = 20$  near the locally stable fixed point which flow there. These box-and-whisker plots display the 0.05, 0.25, 0.5, 0.75, and 0.95 quantiles from a data set of 500 random graphs per condition and 100 Monte Carlo samples of basin size per graph, with notches indicating confidence intervals of the median. The top portions of the boxes are not visible because the median and upper quantiles are all equal to 1. The orange plots shows similar sampling of the fraction of  $\alpha$  space for which the linear approximation holds, determined by the condition  $\|\mathbf{J}(\alpha) - \mathbf{J}(\alpha^{\text{env}})\|_F / \|\mathbf{J}(\alpha^{\text{env}})\|_F = 0.5$ . The orange and cyan dots indicate the means of each distribution. E) Schematic illustration of the thermodynamic constraint on the flow field of the local dynamics.

regulated driving affinity along distinct edges (labeled 1A and 1B in Figure 6A). When the affinity is placed on edge 1A, the system exhibits global stability, with all sampled initial conditions converging to the locally stable fixed point. Additionally, this network is capable of high-dimensional adaptation, as demonstrated in Figure 6B, where perturbations to randomly sampled network parameters result in the system returning to its set point. In this three-dimensional case the adaptation trajectories are notably more complex than those observed in the one-dimensional example of Figure 4D. When the same

network rate matrix is used with the regulated affinity placed on edge 1B, however, the dynamics are no longer globally stable. Instead, the locally stable fixed point has a basin of attraction that does not extend throughout the entire domain, as illustrated by the divergent red trajectories in Figure 6C. Trajectories of  $\alpha(t)$  initiated outside this basin diverge and become unbounded (see SI Figure 13). Additionally, we find that locally stable fixed points become statistically rarer in the space of random networks, although they can be made more common as more feedback connections per edge are added, corre-

sponding to denser matrices  $\mathbf{S}$  (see SI Figures 14 and 15).

Thus, unlike in the previous sections, global stability cannot be guaranteed for all locally stable fixed points when  $N_\alpha = 3$ . Nevertheless, even in cases where the system is not globally stable, we expect that thermodynamic constraints on the non-equilibrium response broaden the basin of attraction beyond what would otherwise be expected. Specifically, we compare the observed basin of attraction to the expected region in which the linear approximation of the Jacobian matrix,  $\mathbf{J}(\alpha^{\text{env}}) \approx \mathbf{J}(\alpha)$ , remains valid. As Figure 6C illustrates, the numerically measured basin of attraction differs significantly from this expectation. In SI Figure 8 we compare these basin sizes across a range of network parameters.

To evaluate the generality of our findings, we analyze randomly generated graphs with 11 nodes and 13 edges, assigning rate matrix parameters at random. For each graph, we introduce up to  $N_\alpha = 5$  feedback loops and identify locally stable fixed points. For each value of  $N_\alpha$ , we sample 500 such fixed points. Around each fixed point, we estimate the size of the basin of attraction using Monte Carlo sampling: 100 trajectories are initialized with random conditions drawn uniformly from a hypercube of side length  $\Delta\alpha = 20$  centered at the fixed point. The basin size is defined as the fraction of this volume from which trajectories converge to the local attractor. We also compare this numerically estimated basin size to the region where a simple linear stability analysis would predict attraction, assuming no special symmetries beyond those of a generic dynamical system. As shown in Figure 6D, although global stability is generally lost for  $N_\alpha > 2$ , the observed basin of attraction remains substantially larger than the prediction from linear theory alone.

We hypothesize that the broadening of the basin of attraction again arises from thermodynamic constraints imposed on the nullclines. Although the basins of attraction do not fill the domain in high-dimensional systems, the local imperfect dynamics have structural features shared with the globally stable, non-local dynamics. In particular, for both types of dynamics, the  $\alpha_a$  component of the full high-dimensional flow  $\dot{\alpha}$  always points toward the locally stable fixed point along the  $\alpha_a$  axis that passes through that point (schematically illustrated in Figure 6E). This directional alignment is a direct consequence of the thermodynamic constraint enforcing monotonicity of the non-equilibrium response (see SI Methods). As a result, it is plausible that the basins of attraction in our locally regulated dynamics are systematically larger than those found in generic dynamical systems of the same dimensionality.

#### IV. DISCUSSION

We have studied the problem of controlling non-equilibrium processes, caricatured generically as Markov

jump processes. Such caricatures are routinely used to model a variety of non-equilibrium biological and synthetic processes. Our results reveal a simple, broadly applicable strategy for achieving tracking and adaptation in non-equilibrium biophysical and synthetic systems through biologically plausible feedback mechanisms. The key to control and adaptation is a thermodynamic constraint that ensures that locally stable feedback connections remain globally stable for up to two regulated driving forces and imposes structural limitations on the global flow field in higher-dimensional systems. While these imperfect local feedback mechanisms do not yield exact solutions to the problems of control and adaptation, they are surprisingly effective across a wide range of conditions and network architectures.

This control framework could be relevant to a range of biophysical processes. For example, adaptive responses of the immune system are thought to near-optimally track the evolution of a diverse range of antigens [1, 39, 40]. Our work could help show how minimal feedback loops which are based on locally estimated antigen binding affinities, ensure that an averaged readout over the antibody sequences robustly reflect the presented antigens. Another key insight from our analysis is the connection between our findings and the general dynamical properties of biochemical adaptation. Specifically, our results are consistent with previous studies on adaptation mechanisms that depend on constraints imposed on the partial derivatives of system variables [6, 7] or on network topology [12, 19–23]. These constraints, which must be assumed to hold in biochemical models of adaptation, establish relationships between response functions and network structure that facilitate integral feedback, enabling perfect adaptation. By contrast, we derive a thermodynamic constraint which, without assuming any other network properties, enforces monotonicity in non-equilibrium responses and allows integral feedback loops to achieve stable regulation without requiring precise parameter tuning. However, we note that the chemical reaction networks that we consider are simplified linear models. Although these results may extend to certain classes of bimolecular reaction networks [30–32], whether such thermodynamic constraints can also be stated and exploited in fully nonlinear chemical dynamics remains to be explored.

Our results can also be compared to the usefulness of imperfect gradients in machine learning, where optimization processes often succeed despite using gradient estimates that only loosely approximate the true global cost function. Techniques such as semi-gradients in temporal difference reinforcement learning (RL) and stochastic mini-batch gradients rely on the fact that even a rough alignment with the true gradient is sufficient for descent [41, 42]. We note that stochastic gradient estimates typically have no systematic errors, whereas other gradient approximations and our imperfect gradients would be expected to. Similarly, methods like contrastive divergence train generative models by estimating equilibrium gradi-

ents using samples from partially converged distributions [43–45]. Even in feed-forward neural networks, backpropagation can tolerate severe approximations; remarkably, networks can still learn effectively when random backward weights replace the true error derivatives, provided that forward passes remain accurate [13–15]. Our work extends these ideas to biophysical systems by showing that in such systems, highly localized and imprecise feedback can still enforce structured, stable dynamics due to fundamental thermodynamic constraints which preserve an overlap with a universal globally stable dynamics.

Finally, our results have broader implications for both synthetic biology and evolutionary theory. The effectiveness of imperfect local feedback raises the possibility that ancestral biological systems may have relied on similarly approximate control mechanisms before refining them through evolutionary processes. This aligns with the idea that evolvability favors simple, modular control structures that are easy to modify and recombine. From a synthetic biology perspective, our findings suggest that designing robust feedback regulation may not require precise circuit engineering, but instead may leverage the inherent constraints of non-equilibrium dynamics to achieve stability and adaptability. This opens the possibility of engineering synthetic biochemical systems with minimal design complexity while still ensuring reliable function; see Refs. 18, 46 for recent examples. Understanding how thermodynamic constraints shape the feasibility of control in biochemical systems could thus provide guiding principles for both studying evolutionary processes and designing biomimetic regulatory networks.

## V. MATERIALS AND METHODS

### A. Mathematical properties of steady state response

Here we consider the effect of varying the non-equilibrium driving  $F_{ij}$  on the steady state occupancy  $\pi_m$  at node  $m$  (see Equation 1). Varying  $F_{ij}$  affects both  $W_{ij}$  and  $W_{ji}$ , and we first pull out the dependence on these rates in the matrix-tree theorem expression for  $\pi_m$  (see Refs. 24, 30 for a description of this theorem). We have

$$\pi_m = \frac{a_m W_{ij} + b_m W_{ji} + c_m}{\bar{a} W_{ij} + \bar{b} W_{ji} + \bar{c}} \quad (11)$$

where

$$a_m = \sum_{T_m}^{(ij)} w^-(T_m) \geq 0 \quad (12)$$

is the sum over all directed spanning trees  $T_m$  rooted at node  $m$  which contain the directed edge  $j \rightarrow i$  (see Figure 2 for an example). The quantity  $w^-(T_m)$  is the product of all edge rates in this tree except for  $W_{ij}$ , which

has been factored out (represented by the  $-$  superscript). Similarly, we have

$$b_m = \sum_{T_m}^{(ji)} w^-(T_m) \geq 0 \quad (13)$$

for the directed spanning trees which include  $i \rightarrow j$ . Note that the directed spanning trees which include  $i \rightarrow j$  necessarily exclude  $j \rightarrow i$ , so the sums in  $a_m$  and  $b_m$  are over separate directed trees. Finally, the sum over directed trees in which neither  $i \rightarrow j$  nor  $j \rightarrow i$  appear is

$$c_m = \sum_{T_m}^{(-)} w(T_m) \geq 0 \quad (14)$$

where the path weights  $w(T_m)$  have no terms factored out. The coefficients in the denominator of Equation 11 include sums over all nodes  $m'$ :

$$\bar{a} = \sum_{m'} a_{m'} > a_m, \quad (15)$$

with  $\bar{b}$  and  $\bar{c}$  defined similarly. From the form in Equation 11 and using the chain rule with  $\partial W_{ij}/\partial F_{ij} = W_{ij}/2$  and  $\partial W_{ji}/\partial F_{ij} = -W_{ji}/2$ , we have

$$\frac{\partial \pi_m}{\partial F_{ij}} = \frac{x_m^{ac} W_{ij} + x_m^{bc} W_{ji} + 2x_m^{ab} W_{ij} W_{ji}}{2(\bar{a} W_{ij} + \bar{b} W_{ji} + \bar{c})^2} \quad (16)$$

where

$$x_m^{ac} = a_m \bar{c} - c_m \bar{a}, \quad (17)$$

$$x_m^{cb} = c_m \bar{b} - b_m \bar{c}, \quad (18)$$

$$x_m^{ab} = a_m \bar{b} - b_m \bar{a}. \quad (19)$$

The sign of Equation 16 is determined by the numerator, which in turn depends on the terms  $x_m^{ac}$ ,  $x_m^{cb}$ , and  $x_m^{ab}$ . We next show that these terms are either all non-negative or all non-positive, implying that the sign of the numerator is fixed for any values of  $W_{ij}$  and  $W_{ji}$  (which as rate matrix elements must be non-negative). The shared sign of these terms follows from our key results (illustrated in Figure 2):

$$a_i = b_j, \quad (20)$$

$$a_j = b_i = 0, \quad (21)$$

and

$$a_i c_m = b_j c_m = c_i a_m + c_j b_m. \quad (22)$$

We prove these relations in the next subsection.

After algebraic manipulation, Equation 22 implies that

$$\frac{x_m^{ac}}{x_m^{ab}} = \frac{c_j}{a_i} \quad (23)$$

and

$$\frac{x_m^{cb}}{x_m^{ab}} = \frac{c_i}{a_i}. \quad (24)$$

Because the right hand sides of Equations 23 and 24 are non-negative, the terms  $x_m^{ac}$ ,  $x_m^{cb}$ , and  $x_m^{ab}$  must share the same sign, proving that the sign of  $\partial\pi_m/\partial F_{ij}$  cannot depend on  $F_{ij}$ . We note that a recent set of results for gradients of  $\pi_m$  in Ref. 25, obtained using linear algebraic manipulations on the rate matrix  $\mathbf{W}$ , also imply the fixed sign derivative result obtained here and can hence be viewed as a complementary derivation.

The sign of  $\partial\pi_m/\partial F_{ij}$  is the same as that of  $x_m^{ab}$  which is in general difficult to predict. However, in the special case  $k = i$  (so that the node of interest is part of the edge of interest), then because  $b_i = 0$  we have  $x_i^{ab} = a_i \bar{b} > 0$  from Equation 22. If  $k = j$  then because  $a_j = 0$  we have  $x_j^{ab} = -b_j \bar{a} < 0$ . Intuitively this agrees with the idea that increasing the flux directly into node  $i$  should increase its steady-state probability.

One can also ask the effect of perturbing edge parameters other than the anti-symmetric term  $F_{ij}$ . From Equation 11 we have (cf. Equation 16)

$$\frac{\partial\pi_m}{\partial W_{ij}} = \frac{x_m^{ac} + x_m^{ab}W_{ji}}{(\bar{a}W_{ij} + \bar{b}W_{ji} + \bar{c})^2} \quad (25)$$

Because  $W_{ji} \geq 0$ , the sign of this derivative is determined by  $x_m^{ac}$  and  $x_m^{ab}$  and is hence fixed across the range of  $W_{ij}$  because  $x_m^{ac}$  and  $x_m^{ab}$  are either both positive or both negative. Similar arguments apply to the derivative  $\partial\pi_m/\partial W_{ji}$ . It has been shown in previous work [24] that the derivative  $\partial\pi_m/\partial E_i$  is

$$\frac{\partial\pi_m}{\partial E_i} = \begin{cases} -\pi_m(1 - \pi_m) & i = m \\ \pi_m\pi_i & i \neq m \end{cases} \quad (26)$$

which has a fixed sign as  $E_i$  is varied. Using our Equation 22, we also have that

$$\frac{\partial\pi_m}{\partial B_{ij}} = \frac{x_m^{ac}W_{ij} - x_m^{cb}W_{ji}}{(\bar{a}W_{ij} + \bar{b}W_{ji} + \bar{c})^2} \quad (27)$$

$$= x_m^{cb}W_{ij} \frac{c_j/c_i - W_{ij}/W_{ji}}{(\bar{a}W_{ij} + \bar{b}W_{ji} + \bar{c})^2}. \quad (28)$$

Since the ratio  $W_{ij}/W_{ji}$  depends on  $E_i$ ,  $E_j$ , and  $F_{ij}$  but not  $B_{ij}$ , then the numerator cannot change sign as  $B_{ij}$  is varied, and this derivative also maintains a fixed sign.

Equations 23 and 24 cause the derivative  $\partial\pi_m/\partial F_{ij}$  to

simplify as

$$\frac{\partial\pi_m}{\partial F_{ij}} = x_m^{ab} \frac{(c_j/a_i)W_{ij} + (c_i/a_i)W_{ji} + 2W_{ij}W_{ji}}{2(\bar{a}W_{ij} + \bar{b}W_{ji} + \bar{c})^2}. \quad (29)$$

The part of this expression which depends on the node index  $m$  is factored out from the part which depends on  $W_{ij}$  and  $W_{ji}$ . In other words, the ratio of any two derivatives

$$\frac{\partial_{F_{ij}}\pi_m}{\partial_{F_{ij}}\pi_{m'}} = \frac{x_m^{ab}}{x_{m'}^{ab}} \equiv R_{m,m'} \quad (30)$$

is independent of  $F_{ij}$ . This means in particular that the derivatives for each  $m$  are extremized at the same value of  $F_{ij}$ . Finally, Equation 30 implies the relationship

$$\pi_m(F_{ij}) = R_{m,m'}\pi_{m'}(F_{ij}) + \pi_{m'}^0, \quad (31)$$

where  $\pi_{m'}^0$  is independent of  $F_{ij}$ . We then have

$$\begin{aligned} \frac{\partial}{\partial F_{ij}} \frac{\pi_m}{\pi_{m'}} &= \frac{\pi_{m'}\partial_{F_{ij}}\pi_m - \pi_m\partial_{F_{ij}}\pi_{m'}}{(\pi_{m'})^2} \\ &= \frac{\pi_m^0}{(\pi_{m'})^2} \frac{\partial\pi_{m'}}{\partial F_{ij}} \end{aligned} \quad (32)$$

which also maintains a fixed sign as  $F_{ij}$  is varied.

## B. Proof of Equations 20-22

Equation 20 can be established as follows. The term  $a_i$  represents the sum over all directed trees rooted at node  $i$  and containing the edge  $j \rightarrow i$ . By flipping this edge, each of these trees can be converted into a directed spanning tree rooted at node  $j$  and containing the edge  $i \rightarrow j$ , which is a unique term in the sum  $b_j$ . The weights  $W_{ij}$  and  $W_{ji}$  of the flipped edges are excluded from  $a_i$  and  $b_j$ , respectively, and as a result these terms both represent the weights for the same collection of edge rates corresponding to flows into nodes  $i$  and  $j$ .

Equation 21 follows from the fact that no directed spanning trees rooted at node  $j$  can contain the edge  $j \rightarrow i$ , and no directed spanning trees rooted at node  $i$  can contain the edge  $i \rightarrow j$ .

Equation 22 can be established as follows. The first equality is due to Equation 20. Inserting the definitions



of the quantities in Equation 22, it reads

$$\begin{aligned}
\sum_{T_i} \sum_{T'_m}^{(ij) \ (-)} w^-(T_i) w(T'_m) &= \sum_{T_j} \sum_{T'_m}^{(ji) \ (-)} w^-(T_j) w(T'_m) \\
&= \sum_{S_m} \sum_{S'_i}^{(ij) \ (-)} w^-(S_m) w(S'_i) \\
&\quad + \sum_{U_m} \sum_{U'_j}^{(ji) \ (-)} w^-(U_m) w(U'_j). \quad (33)
\end{aligned}$$

Let  $N_{[ij]}$  denote the number of undirected spanning trees containing the edge  $i \leftrightarrow j$  and  $N_-$  denote the number of undirected spanning trees without this undirected edge. Let  $N_{ij}^m$  denote the number of directed spanning trees rooted at node  $m$  which contain the directed edge  $j \rightarrow i$ , and similarly for  $N_{ji}^m$ . We have  $N_{ij}^m + N_{ji}^m = N_{[ij]}$  for any  $m$ . The double sum on the left hand side of Equation 33 has  $N_{[ij]}N_-$  terms, while the first double sum on the right hand side has  $N_{ij}^m N_-$  and the second has  $N_{ji}^m N_-$ . Hence, there are the same number of terms on both sides of the equation. If we can find a one-to-one correspondence between the terms on each side of this equation, the equality would be proved. Fortunately, just such a correspondence was illustrated in Ref. 24 using a procedure called “tree surgery.” This procedure algorithmically takes as input a pair of directed spanning trees  $T_m$ , which is rooted at node  $m$  and contains either the edge  $i \leftarrow j$  (or  $j \leftarrow i$ ), and  $T'_n$ , which is rooted at node  $n$  does not contain either edge. The procedure converts this pair into a new pair  $\tilde{T}_n$  and  $\tilde{T}'_m$ , where  $\tilde{T}_n$  contains edge  $i \leftarrow j$  (or  $j \leftarrow i$ ), and  $\tilde{T}'_m$  does not. It was further shown that the weight products  $w(T_m)w(T'_n)$  and  $w(\tilde{T}_n)w(\tilde{T}'_m)$  will be equal if, during the conversion procedure, the edge  $i \leftarrow j$  or  $j \leftarrow i$  is not flipped. Using this procedure, it is possible to convert each of the  $N_{[ij]}N_-$  terms on the left hand side of Equation 33 into either a term of the form  $w^-(S_m)w(S'_i)$ , or one of the form  $w^-(U_m)w(U'_j)$ . This is illustrated in SI Figure 7C. In our case, one can ignore the effect of flipping the distinguished edge  $i \leftrightarrow j$  because doing so would simply convert a tree  $T_i$  rooted at  $i$  into a tree  $T_j$  rooted at  $j$ , or vice versa. The weights of interest  $w^-(T_i) = w^-(T_j)$  for two such trees must be the same because the term  $W_{ij}$  in  $w(T_i)$  and  $W_{ji}$  in  $w(T_j)$ , which would change during the edge flip, have been factored out in  $w^-(T_i)$  and  $w^-(T_j)$ . As a result, flipping the edge  $i \leftarrow j$  does not affect the equality of edge weights between the left and right hand sides of Equation 33. We can therefore establish the desired one-to-one correspondence between the terms on both sides of Equation 33, implying equality.

### C. General formulation of feedback dynamics

For arbitrary  $N_\alpha$  we write the adiabatic dynamics for  $\alpha \in \mathbb{R}^{N_\alpha}$  taking feedback from the network state as

$$\dot{\alpha} = \mathbf{M}(\alpha)(\mathbf{C}(\pi(\alpha)) - \mathbf{C}^{\text{env}}), \quad (34)$$

where  $\mathbf{C} \in \mathbb{R}^{N_C}$  is a vector of network observables, and  $\mathbf{M} \in \mathbb{R}^{N_\alpha \times N_C}$  is a matrix that will be specified below. Defining the Jacobian matrix  $\mathbf{J}(\alpha) \equiv \nabla_\alpha \mathbf{C}(\alpha) \in \mathbb{R}^{N_\alpha \times N_C}$ , we can linearize these dynamics around the fixed point  $\alpha^{\text{env}}$ , for which  $\mathbf{C}(\pi(\alpha^{\text{env}})) = \mathbf{C}^{\text{env}}$ , obtaining

$$\dot{\alpha} \approx \mathbf{M}(\alpha^{\text{env}})\mathbf{J}^\top(\alpha^{\text{env}})(\alpha - \alpha^{\text{env}}). \quad (35)$$

Stability depends on  $\mathbf{M}(\alpha^{\text{env}})\mathbf{J}^\top(\alpha^{\text{env}})$  and its eigenvalues.

To ensure global stability of Equation 34 we can choose  $\mathbf{M}(\alpha) = -\mathbf{J}(\alpha)$ . This choice is non-local because it requires knowledge of the Jacobian elements  $J_{a1} = \frac{\partial C_1}{\partial \alpha_a}$ , which involve rate matrix parameters across the entire network and vary with  $\alpha$ . Under this choice, we can define the Lyapunov function  $\mathcal{L} = \frac{1}{2}\|\mathbf{C} - \mathbf{C}^{\text{env}}\|^2$ , whose gradient with respect to  $\alpha$  is  $\nabla_\alpha \mathcal{L} = \mathbf{J}(\alpha)(\mathbf{C}(\alpha) - \mathbf{C}^{\text{env}})$ . Equation 34 with  $\mathbf{M}(\alpha) = -\mathbf{J}(\alpha)$  thus flows down the gradient of a Lyapunov function and is hence globally stable.

We can approximate these non-local dynamics by choosing  $\mathbf{M}(\alpha) = \mathbf{S} \sim -\mathbf{J}^\top(\alpha^{\text{env}})$ , where  $\mathbf{S}$  is a sparse constant matrix. The local stability of the approximate dynamics at the steady state is determined by the eigenvalues of the matrix  $\mathbf{S}\mathbf{J}^\top(\alpha^{\text{env}})$ . This matrix has rank at most  $N_\alpha$ , and for local stability all  $N_\alpha$  nonzero eigenvalues must be negative. Achieving this requires two conditions. First,  $\mathbf{S}$  must have full rank, which may fail if two observables redundantly provide feedback to two separate regulated edges (see Figure 5). Second, at least  $N_\alpha$  columns of  $\mathbf{J}^\top(\alpha^{\text{env}})$  must not lie in the kernel of  $\mathbf{S}$ . This condition relates to whether the sparse projection of the network observables,  $\mathbf{C}(\pi(\alpha^{\text{env}}))$ , can be “inverted” to uniquely determine the driving affinities  $\alpha^{\text{env}}$ . While the forward problem, solving for  $\mathbf{C}(\pi(\alpha))$  given  $\alpha$ , has a unique solution for any ergodic graph and any  $\alpha$ , the inverse problem of determining  $\alpha$  from observed steady-state node values  $\mathbf{C}$  can only be uniquely solved for certain choices of observed nodes. We discuss this further in the SI. If network observables are chosen such that they do not allow for uniquely solving  $\alpha(\tilde{\pi})$ , and these are used as the nonzero rows in  $\mathbf{S}$ , then  $\mathbf{S}\mathbf{J}^\top(\alpha^{\text{env}})$  will have rank less than  $N_\alpha$ , compromising stability.

### D. Numerical methods

The steady-states of the dissipative discrete state Markov process were obtained using the matrix-tree theorem. We used Mathematica’s IGraph library to enumer-

ate the directed spanning spanning trees of the reaction graph [47]. The dynamical trajectories were generated using Mathematica’s NDSolve function.

To sample random graphs we draw from the uniform distribution over graphs with  $N_n$  nodes and  $N_e$  edges. We initialize the edge rates  $W_{ij}$  using Equation 1 by drawing the  $N_n + 2N_e$  parameters  $E_i$ ,  $B_{ij}$ ,  $F_{ij}$  from uniform distributions over the ranges  $[-E_R, E_R]$ ,  $[-B_R, B_R]$ , and  $[-F_R, F_R]$  respectively. Unless noted otherwise we take  $E_R = B_R = F_R = 1$  throughout the paper.

## ACKNOWLEDGMENTS

We wish to thank Jordan Horowitz, Menachem Stern, Agnish Kumar Behera, Matthew Du, Billie Meadowcroft, and Nicolas Romeo for helpful discussions. This work was supported mainly by DOE BES Grant DE-SC0019765 to SV and CF. We also acknowledge funding from the Physics Frontier Center for Living Systems funded by the National Science Foundation (PHY-2317138). CF acknowledges support from the University of Chicago through a Chicago Center for Theoretical Chemistry Fellowship. The authors acknowledge the University of Chicago’s Research Computing Center for computing resources.

# Supplementary Information

## I. SUPPLEMENTARY FIGURES

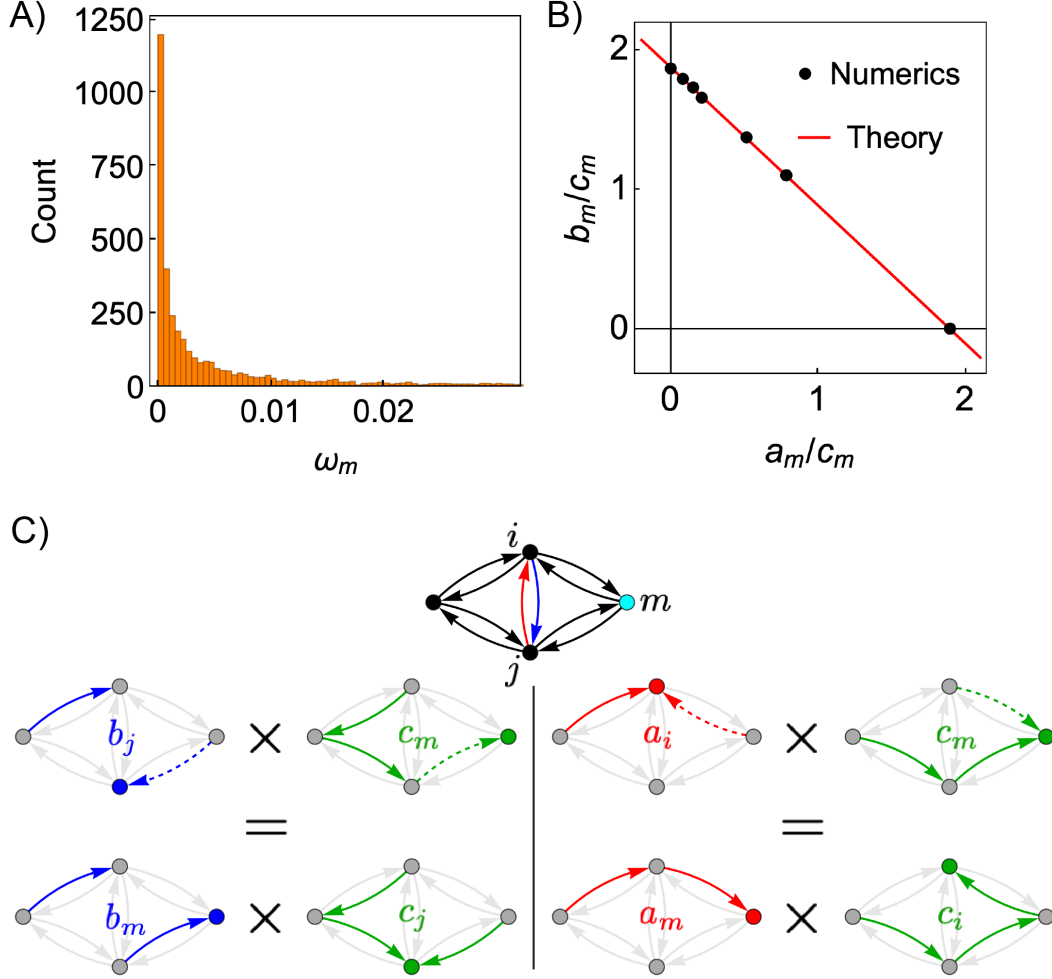


FIG. 7. **Establishing monotonicity of the non-equilibrium response.** A) Histogram of  $\omega_m \equiv (a_m/\bar{a} - c_m/\bar{c})(c_m/\bar{c} - b_m/\bar{b})$ , which will be positive the quantities in Equations 17-19 of the main text are either all positive or all negative, for each node  $m$  of 50 randomly generated graphs. B) Numerical verification of the theoretical result  $b_m/c_m = b_j/c_j - b_j c_i a_m / a_i c_j c_m$ , which is implied by Equation 22 of the main text, for the a node in the graph in Figure 4 of the main text. C) Illustration in a four state graph of the correspondence between terms on both sides of Equation 22 of the main text. Two schematic equations, on the left and right side are depicted. On the left, it is shown how a term from the sum  $b_j c_m$  can be mapped, through swapping of the dashed edges, into a term from  $b_m c_j$ , while on the right it is shown how a term from the sum  $a_i c_m$  can be mapped into a term from  $a_m c_i$ .

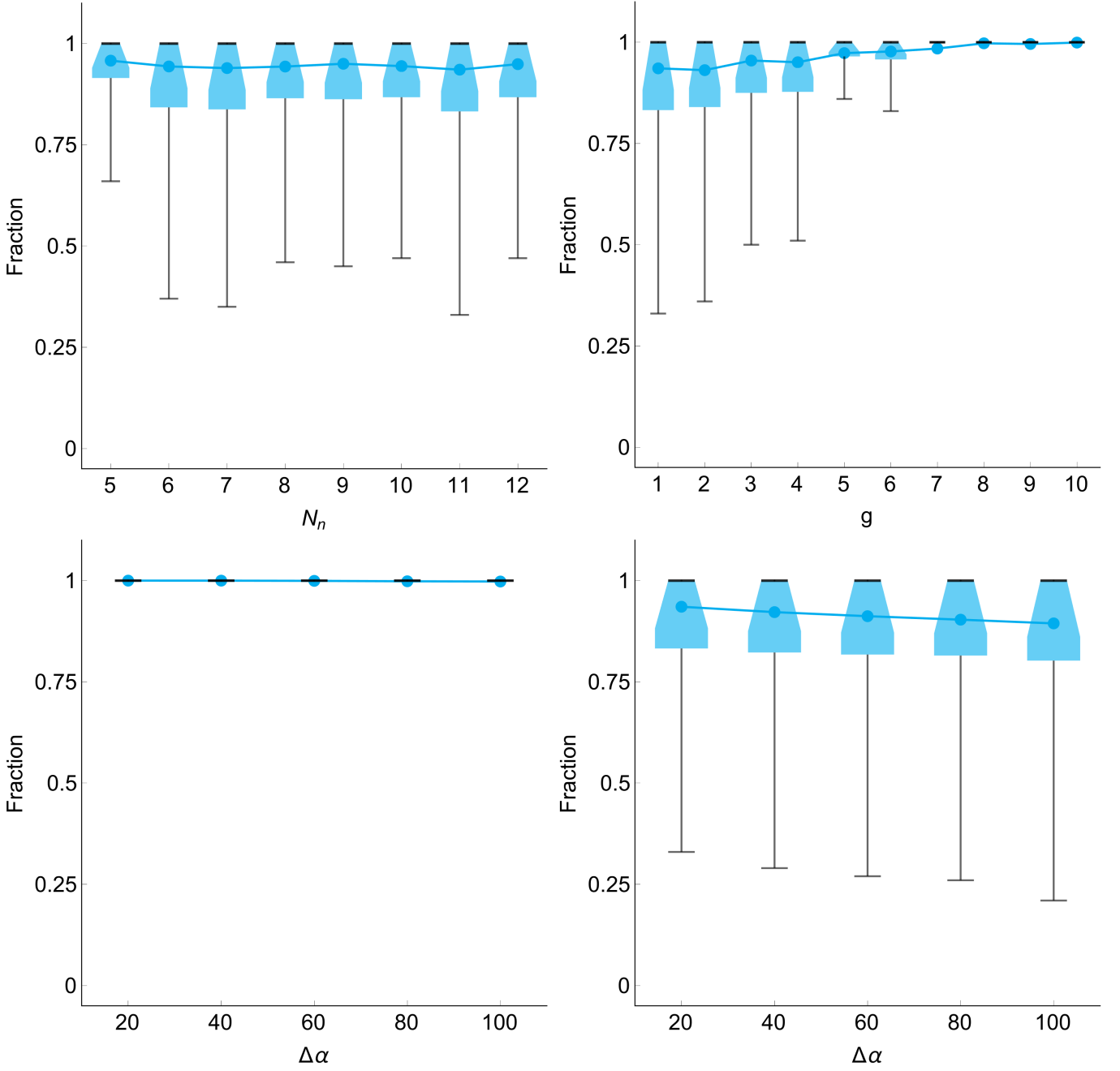


FIG. 8. **Basin of attraction sizes as network parameters vary.** The same procedure used in Figure 6D of the main text is used to estimate the fraction of  $\alpha$  space occupied by the basin of attraction for locally stable fixed points. Unless otherwise specified, the parameters used are  $N_\alpha = 4$ ,  $N_n = 11$ ,  $N_e = 13$ ,  $g = 1$ ,  $E_R = B_R = F_R = 1$ , and  $\Delta\alpha = 20$ , where  $\Delta\alpha$  is the side length of the hypercube in  $\alpha$  explored using Monte Carlo sampling and  $g$  is a sparsity parameter equal to number of non-zero entries per row of  $\mathbf{S}$  when  $\mathbf{C}(\pi) = bp$ . The bottom left panel corresponds to  $N_\alpha = 2$  (confirming global stability as the sampling region is enlarged), while the bottom right corresponds to  $N_\alpha = 4$  (showing weak dependence of the basin size estimates on the size of the sampling region).

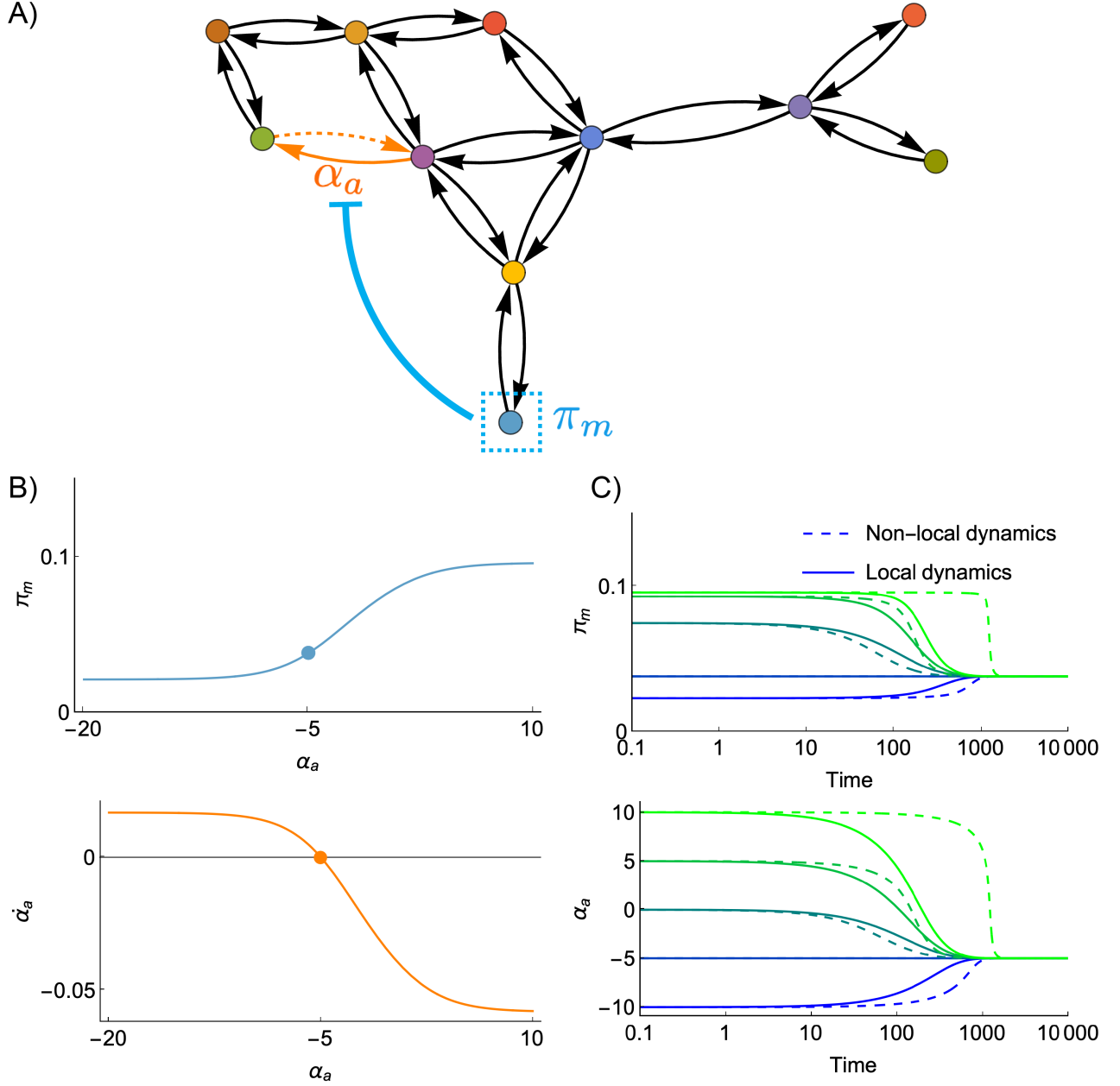


FIG. 9. **One-dimensional learning dynamics.** A) The graph system used in this example with the observable  $C_1 = \pi_m$ . B) *Top*: Plot of the non-equilibrium response  $\pi_m(\alpha_a)$ , with the target value at  $\pi_m^{\text{env}} = \pi_m(-5)$  indicated. *Bottom*: Plot of the adiabatic dynamics  $\dot{\alpha}_a(\alpha_a) = -(\pi_m(\alpha_a) - \pi_m^{\text{env}})$ , indicating global stability. C) *Top*: Trajectories of  $\pi_m$  under the adiabatic local dynamics  $\dot{\alpha}_a(\alpha_a) = -(\pi_m(\alpha_a) - \pi_m^{\text{env}})$  from several initial conditions of  $\alpha_a(t=0)$ . Also plotted are trajectories from the adiabatic non-local dynamics  $\dot{\alpha}_a(\alpha_a) = -(\partial\pi_m(\alpha_a)/\partial\alpha_a)(\pi_m(\alpha_a) - \pi_m^{\text{env}})$  which are always guaranteed to be globally stable. *Bottom*: Trajectories of  $\alpha_a$  corresponding to the top plots.

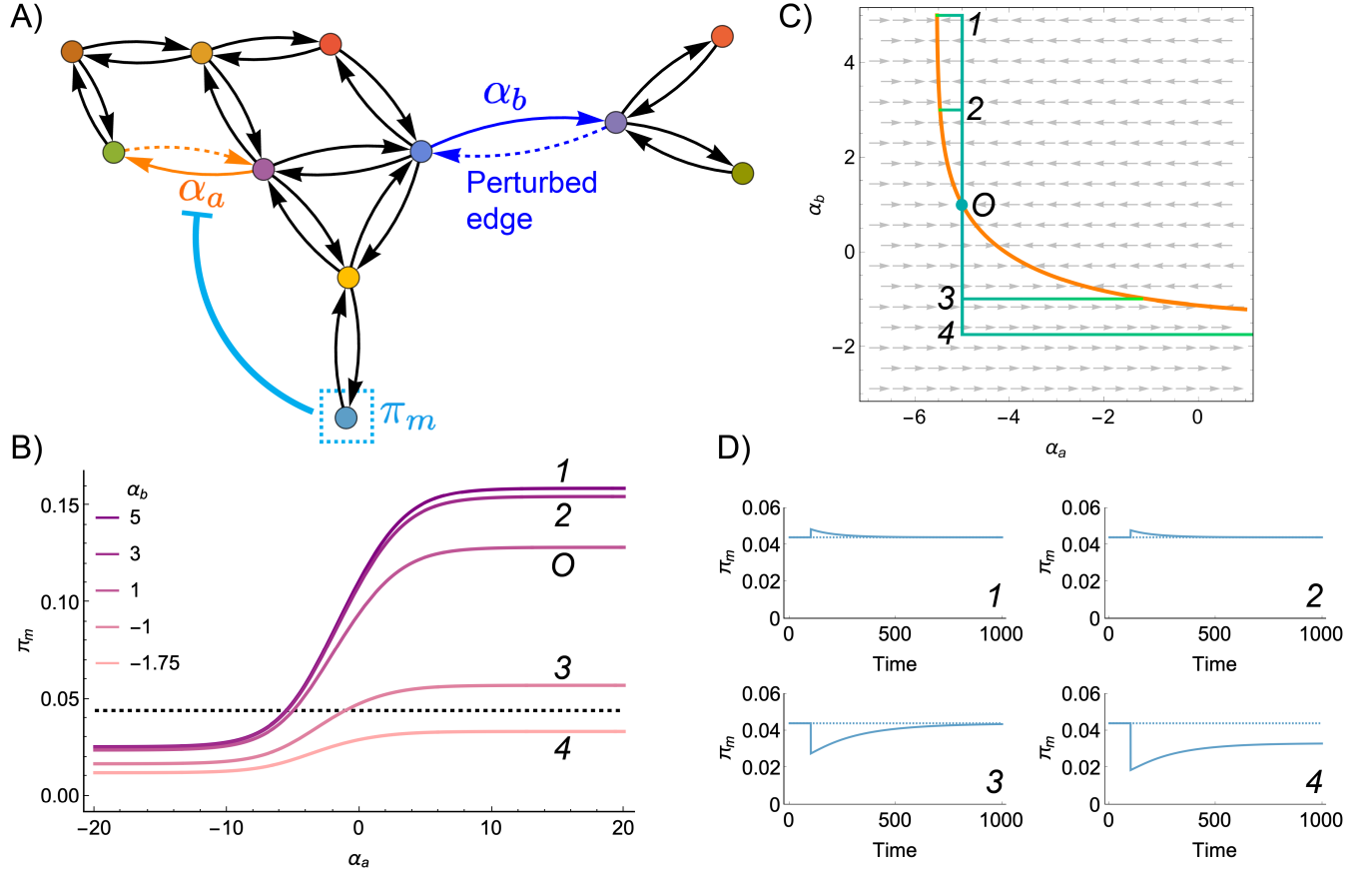


FIG. 10. **Conditional adaptation to changes in network parameters.** A) The graph system used in this example. The blue edge is perturbed as a step change in the remaining panels. B) Plots of the non-equilibrium response  $\pi_m(\alpha_a; \alpha_b)$  for various values of the perturbed edge's driving affinity  $\alpha_b$ . The horizontal dashed line indicates the value  $\pi_m(-5; 1)$ , which all other curves except  $\pi_m(\alpha_a; -1.75)$  intersect. C) Phase plane and trajectories for the one-dimensional adiabatic dynamics  $\dot{\alpha}_a = -(\pi_m(\alpha_a; \alpha_b) - \pi_m^{\text{env}})$  with fixed  $\pi_m^{\text{env}}$  and with various step changes in the perturbed  $\alpha_b$ . For cases 1, 2, and 3, the dynamics flow back to the nullcline, indicating perfect adaptation under the new parameter  $\alpha_b$ , but for case 4 the flow does not intersect the nullcline. D) Same as panel C, but showing the trajectories of  $\pi_m$ .

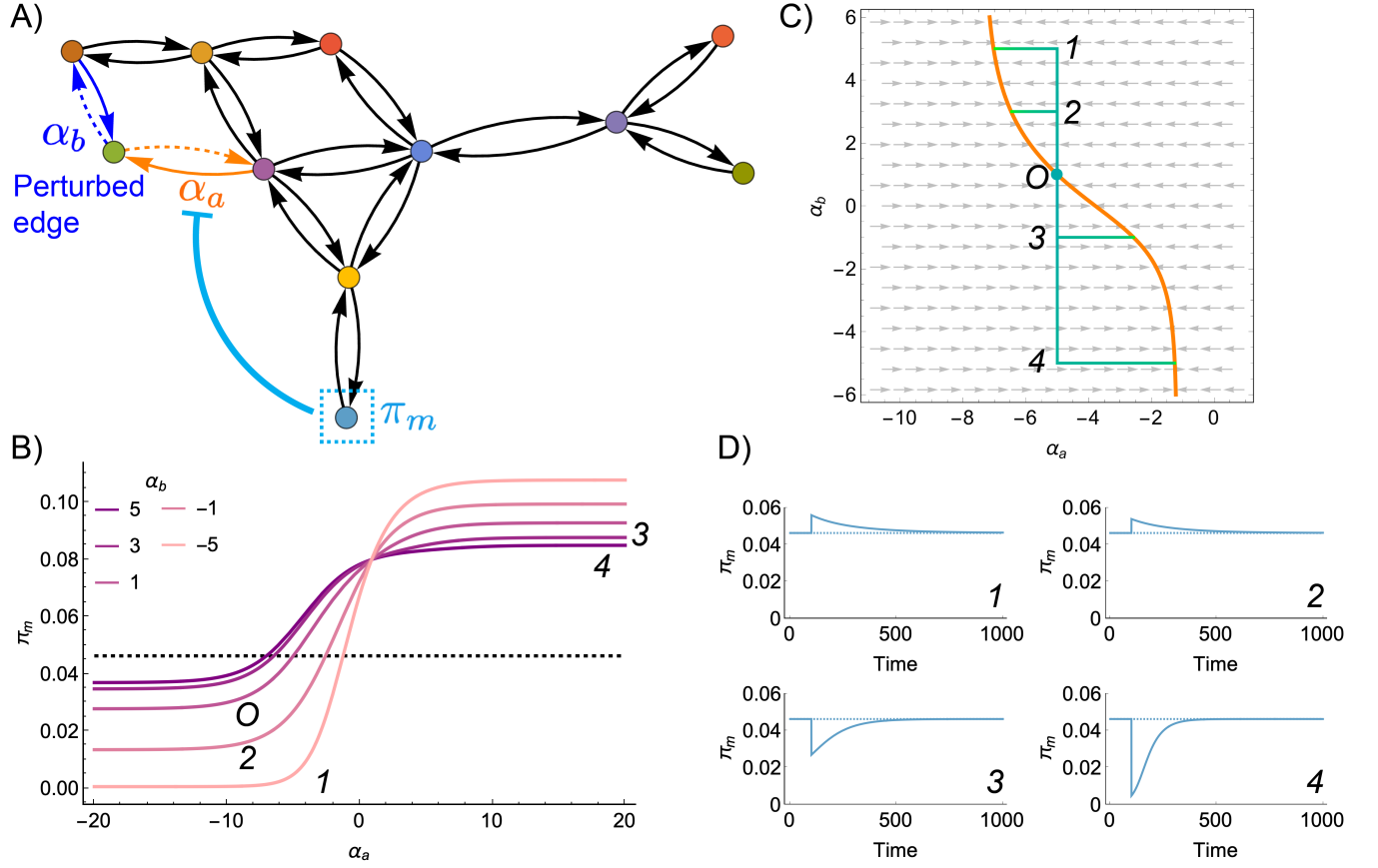


FIG. 11. **Unconditional adaptation to changes in network parameters.** A) The graph system used in this example. The blue edge is perturbed as a step change in the remaining panels. B) Plots of the non-equilibrium response  $\pi_m(\alpha_a; \alpha_b)$  for various values of  $\alpha_b$ . The horizontal dashed line indicates the value of  $\pi_m(-5; 1)$ , which all other curves intersect. C) Phase plane and trajectories for the one-dimensional adiabatic dynamics  $\dot{\alpha}_a = -(\pi_m(\alpha_a; \alpha_b) - \pi_m^{\text{env}})$  with fixed  $\pi_m^{\text{env}}$  and with various step changes in the perturbed  $\alpha_b$ . Due to the structure of the nullcline, all perturbations along  $\alpha_b$  will flow to intersect the nullcline. D) Same as panel C, but showing the trajectories of  $\pi_m$ .



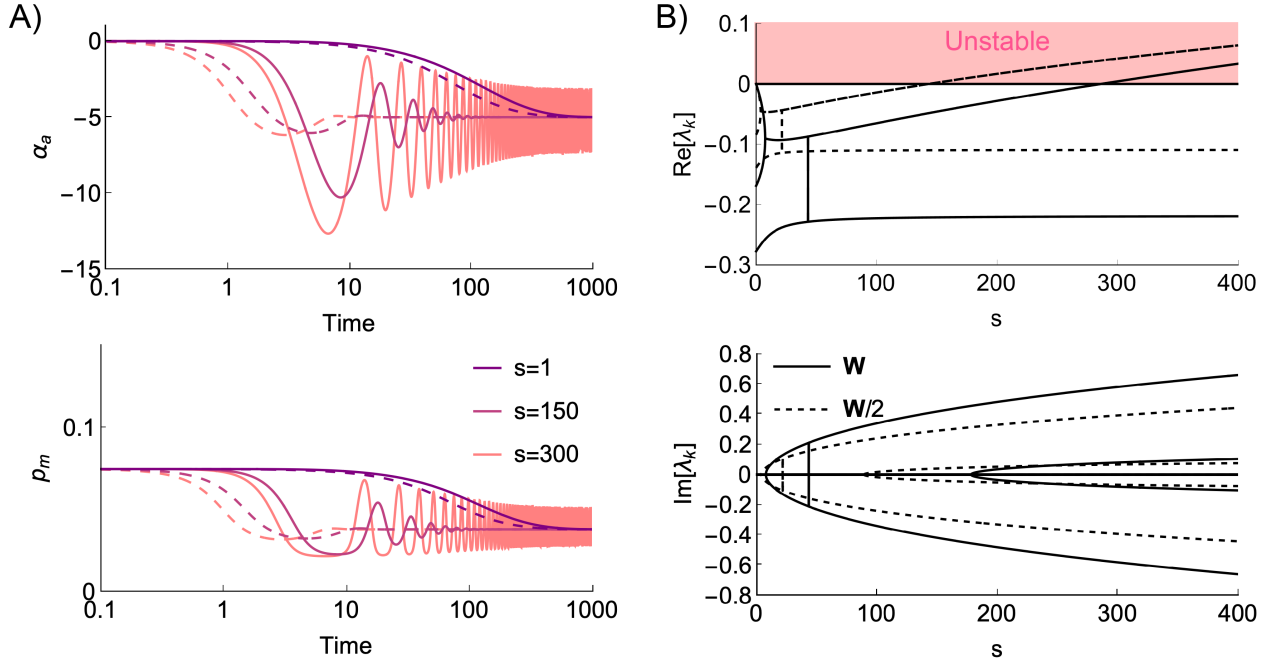


FIG. 12. **Instabilities far outside the adiabatic limit.** A) *Top*: For the graph system in SI Figure 9, plots of trajectories of the non-adiabatic dynamics  $\dot{\alpha}_a(\alpha_a) = -s(p_m - \pi_m^{\text{env}})$ , with  $p_m(t)$  used instead of  $\pi_m(\alpha_a(t))$ , for increasing values of  $s$ . Dashed lines show the non-local non-adiabatic dynamics  $\dot{\alpha}_a(\alpha_a) = -s(\partial p_m / \partial \alpha_a)(p_m - \pi_m^{\text{env}})$ . For the largest value of  $s$ , there are oscillatory instabilities for the local dynamics but not for the non-local dynamics. *Bottom*: Same as the top, but for the corresponding trajectories of  $p_m$ . B) Real part of the eigenspectrum of  $\mathbf{G}_{\text{n.a.}}^{\text{env}}$  (see Equation 37 below) the combined system  $(\dot{\alpha}_a, \mathbf{p}) = \mathbf{G}(\alpha_a, \mathbf{p})$  as  $s$  is increased. An instability occurs when branches of the eigenspectrum take on positive real parts, indicated by the pink region. The dotted lines indicate the eigenspectrum when the rate matrix elements have been halved, thus making the feedback dynamics comparatively faster and the onset of instability lower. *Bottom*: Same as the top, but for the imaginary parts of the eigenspectra.

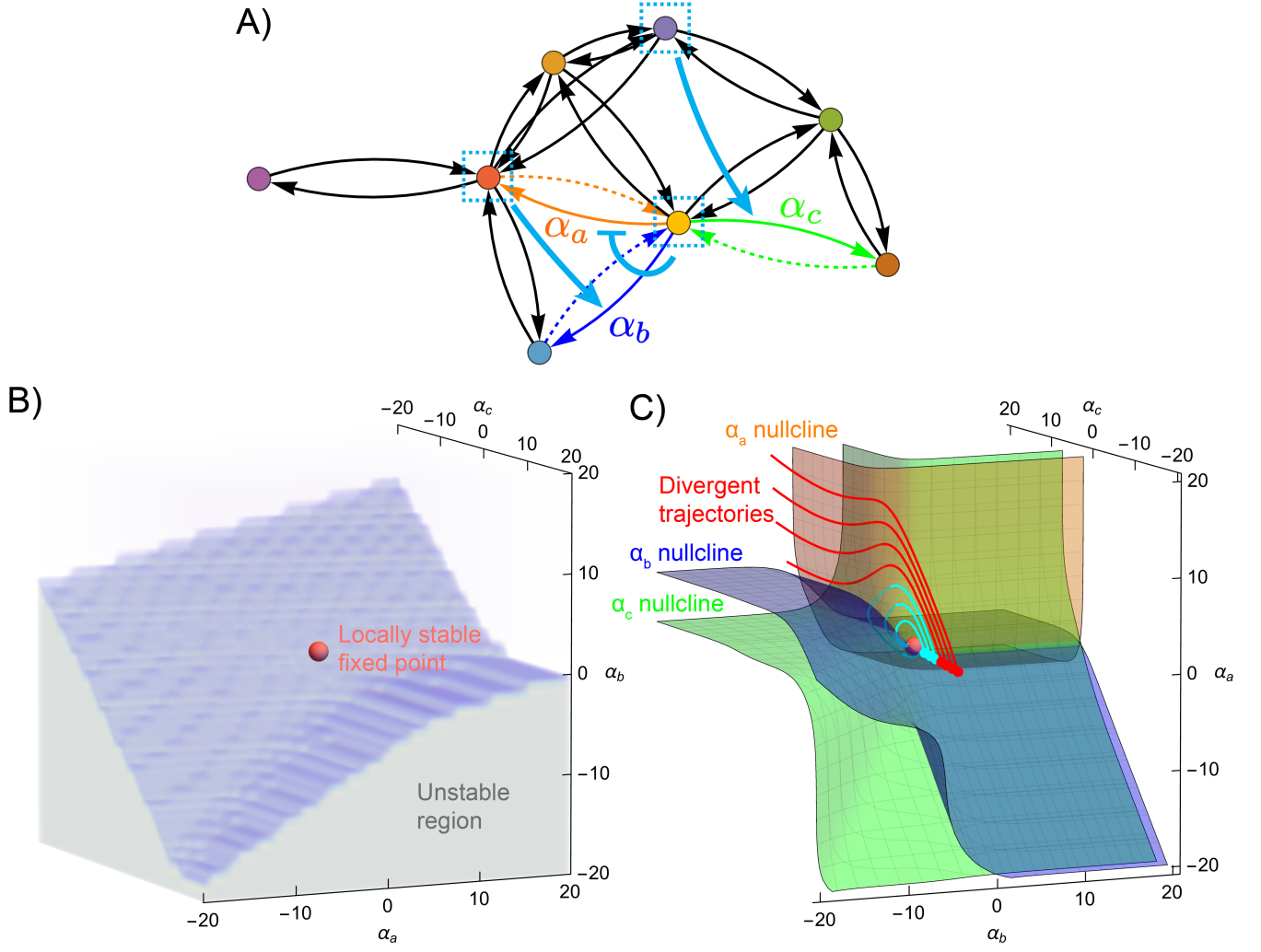


FIG. 13. **Loss of global stability for  $N_\alpha = 3$ .** A) The graph system with  $N_\alpha = 3$  used in this example. B) Plot of the basin of attraction near a locally stable fixed point of the dynamics. Trajectories in the opaque region lie outside the basin and will diverge. C) A different view of the system with the nullclines drawn. Cyan trajectories beginning inside the the basin converge to the fixed point, but red trajectories diverge.

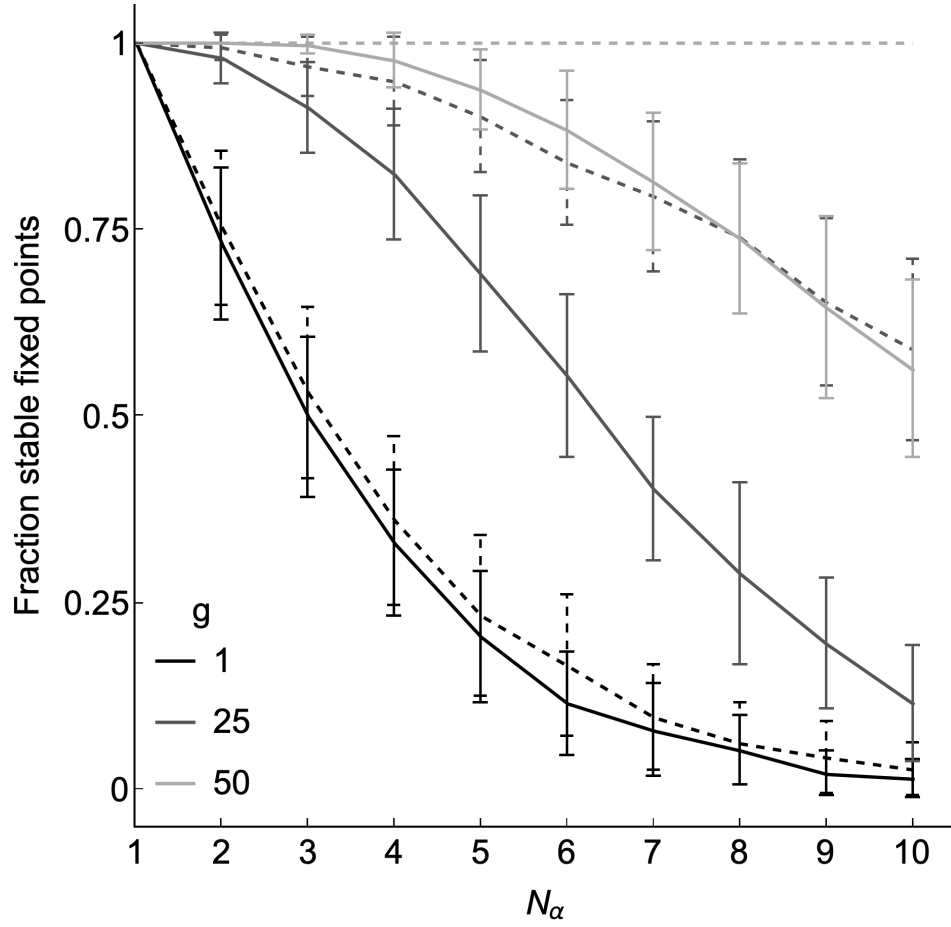


FIG. 14. **Finding locally stable fixed points through sparsity choices.** Plot of the fraction of locally stable fixed points (with all eigenvalues negative) for a scan over random networks. For each value of  $N_\alpha$  we generate 100 random networks by sampling uniformly from the space of graphs with 50 nodes and 75 edges and with edge rate parameters  $E_i$ ,  $B_{ij}$  and  $F_{ij}$  sampled uniformly from the range  $[-1, 1]$ . For each sampled graph, we then draw 20 samples of choices for the regulated edges, the sparse elements of the feedback matrix  $\mathbf{S}$ , and the fixed point  $\boldsymbol{\alpha}^{\text{env}}$ . We find the eigenvalues of  $\mathbf{S}\mathbf{J}^\top$  (see Equation 40 below, with  $\mathbf{C}(\boldsymbol{\pi}) = \boldsymbol{\pi}$ ) at the fixed point. We then compute the fraction of these 20 fixed points which are locally stable and report the average and standard deviation of this fraction over the 100 sampled graphs for this value of  $N_\alpha$ . The sparsity parameter  $g$  determines how many nodes are coupled to each regulated edge in the matrix  $\mathbf{S}$ . The dashed lines are obtained from the same procedure, except  $\mathbf{S}$  is determined using the numerical values of  $-\mathbf{J}^\top$  rather than clipping the elements to  $-1$  or  $1$  depending on their sign. Using these numerical values for  $g = N_n = 50$  yields  $\mathbf{S} = -\mathbf{J}^\top$ , so that the system is guaranteed locally stable because  $\mathbf{S}\mathbf{J}^\top = -\mathbf{J}\mathbf{J}^\top$  is negative definite.

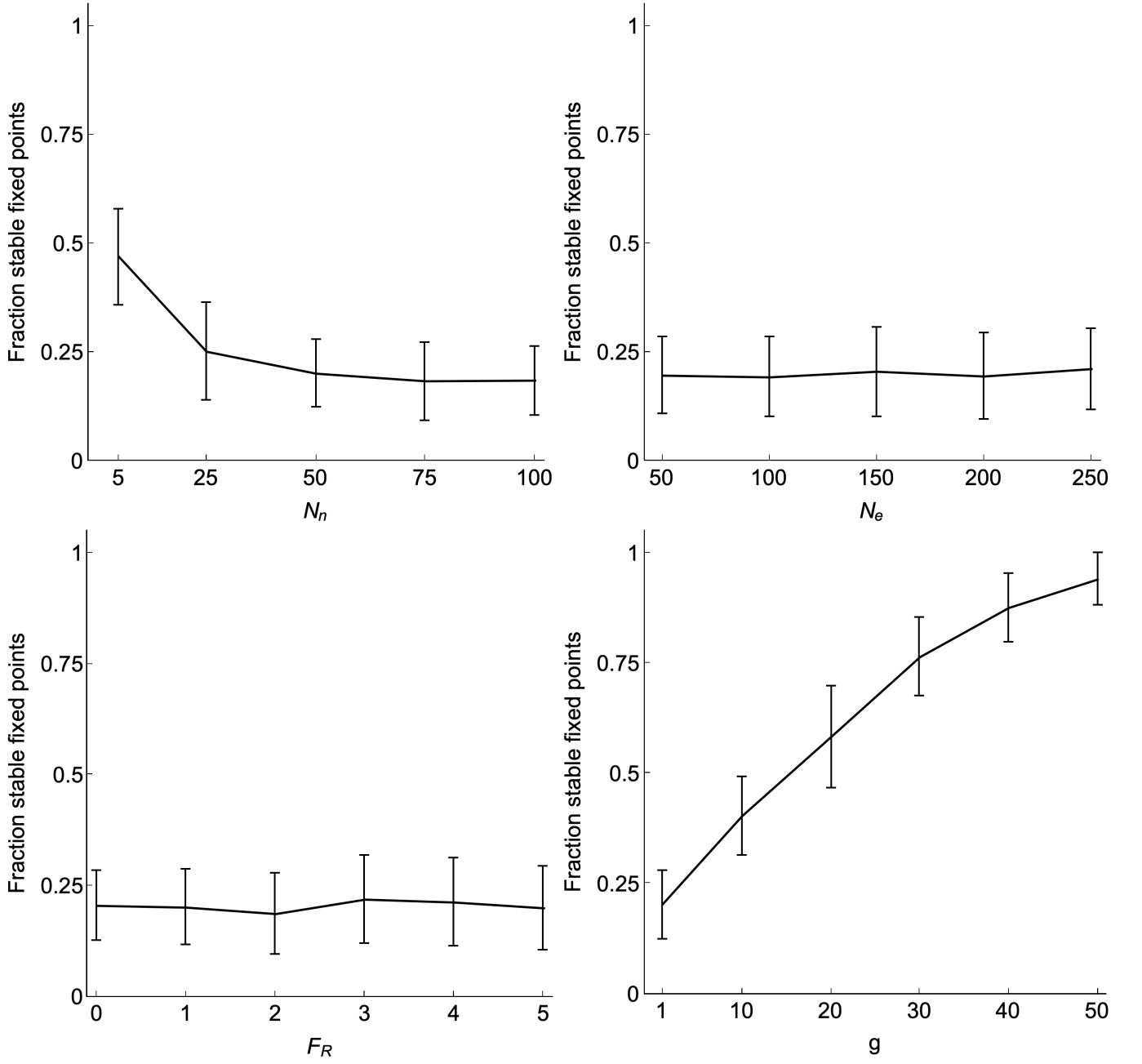


FIG. 15. **Finding locally stable fixed points as network parameters vary.** The same procedure and default parameters as described in the caption to SI Figure 14 is used to estimate the fraction of locally stable fixed points encountered through a scan over random networks.

## II. SUPPLEMENTARY METHODS

### A. Eigenvalues of the combined dynamics

The local non-adiabatic dynamics for the evolution of  $\alpha$  and  $\mathbf{p}$  are given by

$$\begin{pmatrix} \dot{\alpha} \\ \dot{\mathbf{p}} \end{pmatrix} = \begin{pmatrix} \mathbf{S}(\mathbf{C}(\mathbf{p}) - \mathbf{C}^{\text{env}}) \\ \mathbf{W}(\alpha)\mathbf{p} \end{pmatrix} \equiv \mathbf{g}(\alpha, \mathbf{p}). \quad (36)$$

The stability of this system at the fixed point  $(\alpha^{\text{env}}, \pi(\alpha^{\text{env}}))$  depends on the eigenvalues of the matrix

$$\mathbf{G}_{\text{n.a.}}^{\text{env}} = \nabla_{(\alpha, \mathbf{p})} \mathbf{g}(\alpha^{\text{env}}, \pi(\alpha^{\text{env}})), \quad (37)$$

which can be numerically computed but is difficult to study analytically due to the non-linearities of  $\mathbf{g}(\alpha, \mathbf{p})$ .

In the adiabatic limit, the local dynamics reduce to

$$\dot{\alpha} = \mathbf{S}(\mathbf{C}(\pi(\alpha)) - \mathbf{C}^{\text{env}}). \quad (38)$$

The stability of this system at a fixed point  $\alpha^{\text{env}}$  depends on the eigenvalues of

$$\mathbf{G}_{\text{a.}}^{\text{env}} = \nabla_{\alpha} (\mathbf{S}(\mathbf{C}(\pi(\alpha)))) = \mathbf{S} \frac{\partial \mathbf{C}(\pi(\alpha^{\text{env}}))}{\partial \pi} \frac{\partial \pi(\alpha^{\text{env}})}{\partial \alpha}. \quad (39)$$

This can be written more compactly as

$$\mathbf{G}_{\text{a.}}^{\text{env}} = \mathbf{S} \mathbf{J}^{\text{T}}(\alpha^{\text{env}}) \quad (40)$$

where  $\mathbf{J} \in \mathbb{R}^{N_{\alpha} \times N_{\mathcal{C}}} = \nabla_{\alpha} \mathbf{C}(\pi(\alpha))$  is the Jacobian matrix. For simplicity we will in some cases set  $\mathbf{C}(\pi) = \pi$ .

### B. Unique fixed points

Here we consider solutions to the steady-state equation

$$\mathbf{W}(\alpha)\pi = 0 \quad (41)$$

where  $\alpha \in \mathbb{R}^{N_{\alpha}}$ , and we assume that we observe a set of steady-state probabilities  $\{\pi_k\}_{k \in \mathcal{K}}$  where  $\mathcal{K}$  is a set of indices of size  $N_{\alpha}$ . For an ergodic network there is a unique steady state  $\pi$  as a function of  $\mathbf{W}(\alpha)$ , so the mapping from  $\alpha$  to  $\pi$  (the vector with elements  $\{\pi_k\}_{k \in \mathcal{K}}$ ) is a function. We now ask if we can uniquely invert this function.

Equation 41 represents  $N_{\text{n}}$  constraints on the  $N_{\alpha} + N_{\text{n}}$  variables in  $\alpha$  and  $\pi$ , but these constraints are not all independent as the columns of  $\mathbf{W}$  sum to zero. We can supplement these equations with the normalization condition  $\sum_k \pi_k = 1$  to provide  $N_{\text{n}}$  independent constraints. The typical “forward problem” in this setting is that, knowing  $\alpha$ , we use these  $N_{\text{n}}$  constraints to determine the steady-state vector  $\pi$ . We now consider a partial inverse problem: knowing  $\pi \in \mathbb{R}^{N_{\alpha}}$ , we want to determine the  $N_{\text{n}} - N_{\alpha}$  remaining elements of  $\pi$  and the  $N_{\alpha}$  elements of  $\alpha$ . It seems that we should be able to do this because we have enough independent constraints, but the elements of  $\alpha$  enter non-linearly into  $\mathbf{W}(\alpha)$  so we need to check if solutions are unique.

For simplicity we first consider the case  $N_{\alpha} = 1$ , meaning there is one regulated driving force in the direction, say,  $j \rightarrow i$ . Thus  $W_{ij} = W_{ij}^0 e^{\alpha_a/2}$  and  $W_{ji} = W_{ji}^0 e^{-\alpha_a/2}$ . We first reserve the  $i$  and  $j$  rows of Equation 41 and use the remaining  $N_{\text{n}} - 2$  independent constraints to solve for  $N_{\text{n}} - 2$  of the  $N_{\text{n}} - 1$  unknown elements of  $\pi$ , leaving 1 unknown element remaining. It can be shown that the  $i^{\text{th}}$  row of Equation 41 has the form

$$W_{ij}^0 \pi_j e^{\alpha_a/2} - W_{ji}^0 \pi_i e^{-\alpha_a/2} + Q_i = 0 \quad (42)$$

where  $Q_i$  collects several quantities together which do not depend on  $\alpha_a$ . The  $j^{\text{th}}$  row has a similar form

$$-W_{ij}^0 \pi_j e^{\alpha_a/2} + W_{ji}^0 \pi_i e^{-\alpha_a/2} + Q_j = 0. \quad (43)$$

We can now add Equation 42 to Equation 43 to yield  $Q_i = -Q_j$ , which provides the final linear constraint needed to fix the last unknown element of  $\pi$ . Setting  $Q_i = -Q_j$ , we eliminate one of the above two equations and treat the

remaining one as a quadratic function in the unknown quantity  $x_a = e^{\alpha_a/2} > 0$ :

$$W_{ij}^0 \pi_j x_a^2 + Q_i x_a - W_{ji}^0 \pi_i = 0. \quad (44)$$

Regardless of the sign of  $Q_i$ , this quadratic equation has at most 1 change in signs between its ordered coefficients, because the coefficient of  $x_a^2$  is positive while the coefficient of  $x_a$  is negative. By Descartes' rule of signs, this equation thus has at most one positive solution for  $x_a$ . We have therefore found unique solutions for all of the unknown variables.

In the case  $N_\alpha > 1$  the argument proceeds as before. The only new difficulty arises if two driven edges are incident on the same node. To illustrate this we consider the case  $N_\alpha = 2$  with driven edges on  $j \rightarrow i$  and  $k \rightarrow i$ . Reserving rows  $i, j$ , and  $k$  of Equation 41 we can use the  $N_n - 3$  independent constraints to solve for all but one of the unknown elements in  $\boldsymbol{\pi}$ . The  $i, j, k$  rows then read, respectively

$$W_{ij}^0 \pi_j e^{\alpha_a/2} - W_{ji}^0 \pi_i e^{-\alpha_a/2} + Q_i(\alpha_b) = 0, \quad (45)$$

$$-W_{ij}^0 \pi_j e^{\alpha_a/2} + W_{ji}^0 \pi_i e^{-\alpha_a/2} + Q_j = 0, \quad (46)$$

$$-W_{ik}^0 \pi_k e^{\alpha_b/2} + W_{ki}^0 \pi_i e^{-\alpha_b/2} + Q_k = 0. \quad (47)$$

We begin by combining Equations 45 and 46 to eliminate the exponential terms, yielding  $Q_i(\alpha_b) = Q_j$ . This relation allows us to solve for the final unknown component of  $\boldsymbol{\pi}$ . Substituting back into Equation 45, we then solve for the unique positive value of  $\alpha_a$  as a function of  $\alpha_b$ . Finally, we use Equation 47 to determine the unique positive solution for  $\alpha_b$ .

In the arguments above we assumed that the  $N_{n.r.}$  non-reserved rows (which do not involve the regulated edges) can be used to uniquely eliminate  $N_{n.r.}$  degrees of freedom from the  $N_n - N_\alpha$  unknown variables. However, this will not be the case if those rows are not all independent, having low rank. Uniquely inverting the mapping  $\boldsymbol{\alpha} \rightarrow \tilde{\boldsymbol{\pi}}$  thus depends on the specific graph and the choice of  $\mathcal{K}$  and the regulated edges.

### C. Unique roots of $\dot{\alpha}_a$ in the local and non-local local dynamics

Here we consider how many roots the function  $\dot{\alpha}_a$  can have as a function of  $\alpha_a$  for the local and non-local dynamics. This is relevant to understanding shared global features of the flow fields for these two dynamics (see Figure 6E of the main text). For simplicity in this section we assume  $\mathbf{C}(\boldsymbol{\pi}) = \boldsymbol{\pi}$ , but the arguments carry over straightforwardly if the observables  $\mathbf{C}(\boldsymbol{\pi})$  are, for example, arbitrary linear functions of  $\boldsymbol{\pi}$  which also obey the required monotonicity properties (see the main text for details).

For the local dynamics with  $g = 1$ , where  $g$  is the number of non-zero elements per row of the sparse matrix  $\mathbf{S}$ , we have (no summation over  $m$ )

$$\dot{\alpha}_a = S_{am}(\pi_m - \pi_m^{\text{env}}) \quad (48)$$

for some node  $m$ . This function  $\dot{\alpha}$  is strictly monotonic as a function of  $\alpha_a$ , as described in the main text. As a result, it can have at most one intersection with the line  $\dot{\alpha}_a = 0$ . This function is also strictly monotonic as a function of all other  $\alpha_b \neq \alpha_a$ , and therefore has at most one root along any line parallel to the components of  $\boldsymbol{\alpha}$ .

For the case  $g > 1$  the local dynamics are

$$\dot{\alpha}_a = \sum_k S_{ak}(\pi_k - \pi_k^{\text{env}}) \quad (49)$$

where only  $g$  elements  $S_{ak}$  of the  $a^{\text{th}}$  row of  $\mathbf{S}$  are non-zero. This function is also strictly monotonic as a function of all variables  $\alpha_a, \alpha_b, \dots$ . To see this, recall that in main text Equation 30 we show that for any  $k, k'$  the ratio of the derivatives  $\partial \pi_k / \partial \alpha_a$  and  $\partial \pi_{k'} / \partial \alpha_a$  does not depend on  $\alpha_a$ . That is,

$$\frac{\partial}{\partial \alpha_a} \left( \frac{\partial \pi_k / \partial \alpha_a}{\partial \pi_{k'} / \partial \alpha_a} \right) \equiv \frac{\partial}{\partial \alpha_a} R_{k,k'}^a = 0. \quad (50)$$

We thus have, for example,

$$\frac{\partial \dot{\alpha}_a}{\partial \alpha_b} = \sum_k S_{ak} \frac{\partial \pi_k}{\partial \alpha_b} = \frac{\partial \pi_{k'}}{\partial \alpha_b} \sum_k S_{ak} R_{k,k'}^b, \quad (51)$$

where we have factored the derivative for an arbitrary index  $k'$ . Neither of the two factors on the right of Equation 51 can change sign as a function of  $\alpha_b$ , proving monotonicity and therefore uniqueness of roots of  $\dot{\alpha}_a$  along this axis. The same argument applies for the derivatives with respect to any other element of  $\alpha$ .

For the non-local dynamics, we have

$$\dot{\alpha}_a = - \sum_k \frac{\partial \pi_k}{\partial \alpha_a} (\pi_k - \pi_k^{\text{env}}). \quad (52)$$

We can write

$$\dot{\alpha}_a = - \frac{\partial \pi_{k'}}{\partial \alpha_a} \sum_k R_{k,k'}^a (\pi_k - \pi_k^{\text{env}}) = 0. \quad (53)$$

The derivative  $\partial \pi_{k'}/\partial \alpha_a$  has a fixed sign as a function of  $\alpha_a$ , and we can thus ignore this prefactor and look for solutions as a function of  $\alpha_a$  of

$$\sum_k R_{k,k'}^a (\pi_k - \pi_k^{\text{env}}) = 0. \quad (54)$$

This is a sum of strictly monotonic functions  $\pi_k(\alpha_a) - \pi_k^{\text{env}}$  with weights  $R_{k,k'}^a$  which can be positive or negative. The whole sum is also monotonic, because

$$\frac{\partial}{\partial \alpha_a} \sum_k R_{k,k'}^a (\pi_k - \pi_k^{\text{env}}) = \sum_k R_{k,k'}^a \frac{\partial \pi_k}{\partial \alpha_a} = \frac{\partial \pi_{k'}}{\partial \alpha_a} \sum_k (R_{k,k'}^a)^2. \quad (55)$$

The derivative with respect to  $\alpha_a$  thus has the same fixed sign as  $\partial \pi_{k'}/\partial \alpha_a$ . We can write

$$\dot{\alpha}_a = \frac{\partial \pi_{k'}}{\partial \alpha_a} L_{k'}(\alpha_a) \quad (56)$$

where  $L_{k'}(\alpha_a)$  is strictly decreasing or increasing depending on the sign of  $\partial \pi_{k'}/\partial \alpha_a$ . The factor  $L_{k'}(\alpha_a)$  can therefore have at most one root, a feature which it shares with the local dynamics. We note, however, that unlike in the local dynamics there can be multiple roots of  $\dot{\alpha}_a$  as a function of  $\alpha_b \neq \alpha_a$ .

- 
- [1] Andreas Mayer, Vijay Balasubramanian, Aleksandra M Walczak, and Thierry Mora. How a well-adapting immune system remembers. *Proceedings of the National Academy of Sciences*, 116(18):8815–8823, 2019.
  - [2] HH Mattingly, K Kamino, BB Machta, and T Emonet. Escherichia coli chemotaxis is information limited. *Nature physics*, 17(12):1426–1431, 2021.
  - [3] Oskar H Schnaack, Luca Peliti, and Armita Nourmohammad. Learning and organization of memory for evolving patterns. *Physical Review X*, 12(2):021063, 2022.
  - [4] Shamreen Iram, Emily Dolson, Joshua Chiel, Julia Pelesko, Nikhil Krishnan, Özenç Güngör, Benjamin Kuznets-Speck, Sebastian Deffner, Efe Ilker, Jacob G Scott, et al. Controlling the speed and trajectory of evolution with counterdiabatic driving. *Nature Physics*, 17(1):135–142, 2021.
  - [5] Arvind Murugan, Kabir Husain, Michael J Rust, Chelsea Hepler, Joseph Bass, Julian MJ Pietsch, Peter S Swain, Siddhartha G Jena, Jared E Toettcher, Arup K Chakraborty, et al. Roadmap on biology in time varying environments. *Physical biology*, 18(4):041502, 2021.
  - [6] Ganhui Lan, Pablo Sartori, Silke Neumann, Victor Sourjik, and Yuhai Tu. The energy–speed–accuracy trade-off in sensory adaptation. *Nature physics*, 8(5):422–428, 2012.
  - [7] Yuhai Tu and Wouter-Jan Rappel. Adaptation in living systems. *Annual review of condensed matter physics*, 9(1):183–205, 2018.
  - [8] Stefan Landmann, Caroline M Holmes, and Mikhail Tikhonov. A simple regulatory architecture allows learning the statistical structure of a changing environment. *Elife*, 10:e67455, 2021.
  - [9] Herbert B. Callen. *Thermodynamics and an Introduction to Thermostatistics*. John Wiley & Sons, 1991.
  - [10] Sara D Mahdavi, Gabriel L Salmon, Patill Daghljan, Hernan G Garcia, and Rob Phillips. Flexibility and sensitivity in gene regulation out of equilibrium. *Proceedings of the National Academy of Sciences*, 121(46):e2411395121, 2024.
  - [11] Domitilla Del Vecchio and Richard M Murray. *Biomolecular feedback systems*. Princeton University Press Princeton, NJ, 2015.
  - [12] Wenzhe Ma, Ala Trusina, Hana El-Samad, Wendell A Lim, and Chao Tang. Defining network topologies that can achieve



- biochemical adaptation. *Cell*, 138(4):760–773, 2009.
- [13] Timothy P Lillicrap, Daniel Cownden, Douglas B Tweed, and Colin J Akerman. Random synaptic feedback weights support error backpropagation for deep learning. *Nature communications*, 7(1):13276, 2016.
  - [14] Timothy P Lillicrap, Adam Santoro, Luke Marris, Colin J Akerman, and Geoffrey Hinton. Backpropagation and the brain. *Nature Reviews Neuroscience*, 21(6):335–346, 2020.
  - [15] Logan G Wright, Tatsuhiro Onodera, Martin M Stein, Tianyu Wang, Darren T Schachter, Zoey Hu, and Peter L McMahon. Deep physical neural networks trained with backpropagation. *Nature*, 601(7894):549–555, 2022.
  - [16] Uri Alon. *An introduction to systems biology: design principles of biological circuits*. Chapman and Hall/CRC, 2019.
  - [17] Nagarajan Nandagopal and Michael B Elowitz. Synthetic biology: integrated gene circuits. *science*, 333(6047):1244–1248, 2011.
  - [18] Zibo Chen, James M Linton, Shiyu Xia, Xinwen Fan, Dingchen Yu, Jinglin Wang, Ronghui Zhu, and Michael B Elowitz. A synthetic protein-level neural network in mammalian cells. *Science*, 386(6727):1243–1250, 2024.
  - [19] Robyn P Araujo and Lance A Liotta. The topological requirements for robust perfect adaptation in networks of any size. *Nature communications*, 9(1):1757, 2018.
  - [20] Robyn P Araujo and Lance A Liotta. Universal structures for adaptation in biochemical reaction networks. *Nature Communications*, 14(1):2251, 2023.
  - [21] Stephanie K Aoki, Gabriele Lillacci, Ankit Gupta, Armin Baumschlager, David Schweingruber, and Mustafa Khammash. A universal biomolecular integral feedback controller for robust perfect adaptation. *Nature*, 570(7762):533–537, 2019.
  - [22] Yuji Hirono, Ankit Gupta, and Mustafa Khammash. Rethinking robust adaptation: Characterization of structural mechanisms for biochemical network robustness through topological invariants. *PRX Life*, 3:013017, Mar 2025.
  - [23] Corentin Briat, Ankit Gupta, and Mustafa Khammash. Antithetic integral feedback ensures robust perfect adaptation in noisy biomolecular networks. *Cell systems*, 2(1):15–26, 2016.
  - [24] Jeremy A Owen, Todd R Gingrich, and Jordan M Horowitz. Universal thermodynamic bounds on nonequilibrium response with biochemical applications. *Physical Review X*, 10(1):011066, 2020.
  - [25] Timur Aslyamov and Massimiliano Esposito. Nonequilibrium response for markov jump processes: Exact results and tight bounds. *Physical Review Letters*, 132(3):037101, 2024.
  - [26] Gabriela Fernandes Martins and Jordan M. Horowitz. Topologically constrained fluctuations and thermodynamics regulate nonequilibrium response. *Phys. Rev. E*, 108:044113, Oct 2023.
  - [27] Jürgen Schnakenberg. Network theory of microscopic and macroscopic behavior of master equation systems. *Reviews of Modern physics*, 48(4):571, 1976.
  - [28] Tau-Mu Yi, Yun Huang, Melvin I Simon, and John Doyle. Robust perfect adaptation in bacterial chemotaxis through integral feedback control. *Proceedings of the National Academy of Sciences*, 97(9):4649–4653, 2000.
  - [29] Matthew A Reyer, Shriram Chennakesavalu, Emily M Heideman, Xiangqian Ma, Magda Bujnowska, Lu Hong, Aaron R Dinner, Carin K Vanderpool, and Jingyi Fei. Kinetic modeling reveals additional regulation at co-transcriptional level by post-transcriptional srna regulators. *Cell reports*, 36(13), 2021.
  - [30] Jeremy Gunawardena. A linear framework for time-scale separation in nonlinear biochemical systems. *PloS one*, 7(5):e36321, 2012.
  - [31] Kee-Myoung Nam, Rosa Martinez-Corral, and Jeremy Gunawardena. The linear framework: using graph theory to reveal the algebra and thermodynamics of biomolecular systems. *Interface Focus*, 12(4):20220013, 2022.
  - [32] Jeremy A Owen, Pranay Talla, John W Biddle, and Jeremy Gunawardena. Thermodynamic bounds on ultrasensitivity in covalent switching. *Biophysical Journal*, 122(10):1833–1845, 2023.
  - [33] Naama Barkai and Stan Leibler. Robustness in simple biochemical networks. *Nature*, 387(6636):913–917, 1997.
  - [34] John Bechhoefer. *Control theory for physicists*. Cambridge University Press, 2021.
  - [35] Lawrence Perko. *Differential equations and dynamical systems*, volume 7. Springer Science & Business Media, 2013.
  - [36] Eugene M Izhikevich. *Dynamical systems in neuroscience*. MIT press, 2007.
  - [37] Edward Ott. *Chaos in dynamical systems*. Cambridge university press, 2002.
  - [38] Lacramioara Bintu, N.E. Buchler, Hernan G. Garcia, U. Gerland, T. Hwa, J. Kondev, and R. Phillips. Transcriptional regulation by the numbers: models. *Current Opinion in Genetics & Development*, 15(2):116–124, 2005.
  - [39] Thomas B Kepler and Alan S Perelson. Somatic hypermutation in b cells: an optimal control treatment. *Journal of theoretical biology*, 164(1):37–64, 1993.
  - [40] Armita Nourmohammad and Ceyhan Eksin. Optimal evolutionary control for artificial selection on molecular phenotypes. *Physical Review X*, 11(1):011044, 2021.
  - [41] Yann LeCun, Yoshua Bengio, and Geoffrey Hinton. Deep learning. *nature*, 521(7553):436–444, 2015.
  - [42] Richard S Sutton and Andrew G Barto. *Reinforcement learning: An introduction*. MIT press, 2018.
  - [43] Miguel A Carreira-Perpinan and Geoffrey Hinton. On contrastive divergence learning. In *International workshop on artificial intelligence and statistics*, pages 33–40. PMLR, 2005.
  - [44] Aurélien Decelle, Cyril Furtlehner, and Beatriz Seoane. Equilibrium and non-equilibrium regimes in the learning of restricted boltzmann machines. *Advances in Neural Information Processing Systems*, 34:5345–5359, 2021.
  - [45] Elisabeth Agoritsas, Giovanni Catania, Aurélien Decelle, and Beatriz Seoane. Explaining the effects of non-convergent mcmc in the training of energy-based models. In *International Conference on Machine Learning*, pages 322–336. PMLR, 2023.
  - [46] Xiaoyu Yang, Jason W Rocks, Kaiyi Jiang, Andrew J Walters, Kshitij Rai, Jing Liu, Jason Nguyen, Scott D Olson, Pankaj Mehta, James J Collins, et al. Engineering synthetic phosphorylation signaling networks in human cells. *Science*, 387(6729):74–81, 2025.

- [47] Szabolcs Horvát, Jakub Podkalicki, Gábor Csárdi, Tamás Nepusz, Vincent Traag, Fabio Zanini, and Daniel Noom. Igraph/m: graph theory and network analysis for mathematica. *Journal of Open Source Software*, 8(81):4899, 2023.